Fluid-rock interaction, skarn genesis, and hydrothermal alteration within an upper crustal fault zone (Island of Elba, Italy)

Paolo S. Garofalo [a,*], Jacopo Maffei [a], Samuele Papeschi [b], Francesco Dellisanti [c], Christoph Neff [d], Gunnar Schwarz [d], Peter Keresztes Schmidt [d,e], Detlef Günther [d]

[a] *Dipartimento di Scienze Biologiche, Geologiche Ambientali, Università di Bologna, Italy*
[b] *Kochi Institute for Core Sample Research (X-Star), Japan Agency for Marine-Earth Science and Technology (JAMSTEC), Nankoku, Japan*
[c] *Analitica - Materials Research Laboratory, San Lazzaro di Savena, Bologna, Italy*
[d] *ETH Zurich, Department of Chemistry and Applied Biosciences, Laboratory of Inorganic Chemistry, Zurich, Switzerland*
[e] *Space Research and Planetary Sciences, Physics Institute, University of Bern, 3012 Bern, Switzerland[1]*

ARTICLE INFO

ABSTRACT

The Terranera magnetite-hematite-pyrite deposit of the Island of Elba (Italy) is an historical skarn deposit hosted by a fault zone of regional importance (Zuccale Fault) and by its hanging wall rocks.

We combine field observations with petrographic data, electron probe microanalyses (EPMA), XRPD data, fluid inclusion microthermometry, and element imaging by Laser Ablation-Inductively Coupled Plasma-Time of Flight Mass Spectrometry (LA-ICP-TOFMS) to define the ore-forming process at Terranera. We show that in this location the fault is made of four levels of mineralized fault rocks having distinct mineral compositions. In these levels, a mineral association made of diopside, clinozoisite, and other Mg-rich minerals is replaced by magnetite, hematite, pyrite, Mg-hornblende, clinochlore, and other Mg-rich phyllosilicates. This paragenesis is overprinted by goethite and clay minerals. Chlorite-quartz geothermometry and fluid inclusion microthermometry show that ore precipitation occurred at 350–180 °C from fluids of distinct bulk salinities, but goethite and clay mineral overprinting progressed at lower T.

We propose that Terranera is a magnesian Fe skarn formed due to the interaction between distinct hydrothermal fluids and a dolomitic protolith, which was preserved within the fault zone. These fluids mixed and cooled during protolith metasomatism, causing ore precipitation due to oxidation and desulfidation. A very similar process was described in a large deposit of Elba (Rio Marina). Argillic alteration was widespread within the fault but met permanently intermediate sulfidation conditions. Trace element composition of hematite shows that Terranera has features that overlap those of skarn and epithermal deposits. In particular, elements that are typical of epithermal deposits (Sb, Ga, Ge, As) occur at mass fractions (50–200 μg/g) that are either unreported or not typical of hematite from skarn deposits. These features identify Terranera as formed in an ore environment that was transitional between that of a skarn and of an epithermal deposit. These features are shared by other historical deposits located at Elba and in the massive pyritic ore district of south Tuscany (e.g., Gavorrano, Fenice Capanne). This indicates that a similar environment might have occurred during the Neogene beyond Elba, in a much larger ore district of south Tuscany.

1. Introduction

Faults are important fluid conduits of the Earth's crust and control many ore-forming processes (Oliver and Bons, 2001). Their fundamental role was defined for a large number of ore deposits, including the vein-hosted orogenic Au (Garofalo et al., 2002; Groves et al., 2018), the

magmatic hydrothermal (Thompson et al., 1999), and the porphyry-epithermal deposits (Muntean and Einaudi, 2001). In skarn deposits, hydraulic fracturing generated by shallow-level intrusions increases the permeability of the host rocks, and as a consequence faults are the preferential sites of retrograde skarn formation (Meinert et al., 2005). In the distal sections of skarns, fault networks control the establishment of

"fluid escape structures", which are used as exploration tools (Meinert et al., 2005).

Hence, fracturing, hydrothermal fluid flow, and ore formation occur at the same time in many ore systems; however, the fluid-fault inter-action processes that steer ore formation are poorly constrained. In skarn deposits, calc-silicates and ore minerals often obliterate the

pristine fault rocks. Thus, little of the pristine fault fabric survive host rock metasomatism and the fundamental ore-forming processes occur-ring within faults cannot be defined.

In this work, we combine field observations with a multi-analytical dataset made of petrographic data, electron probe microanalyses, X-ray powder diffraction analyses, fluid inclusion microthermometry, and
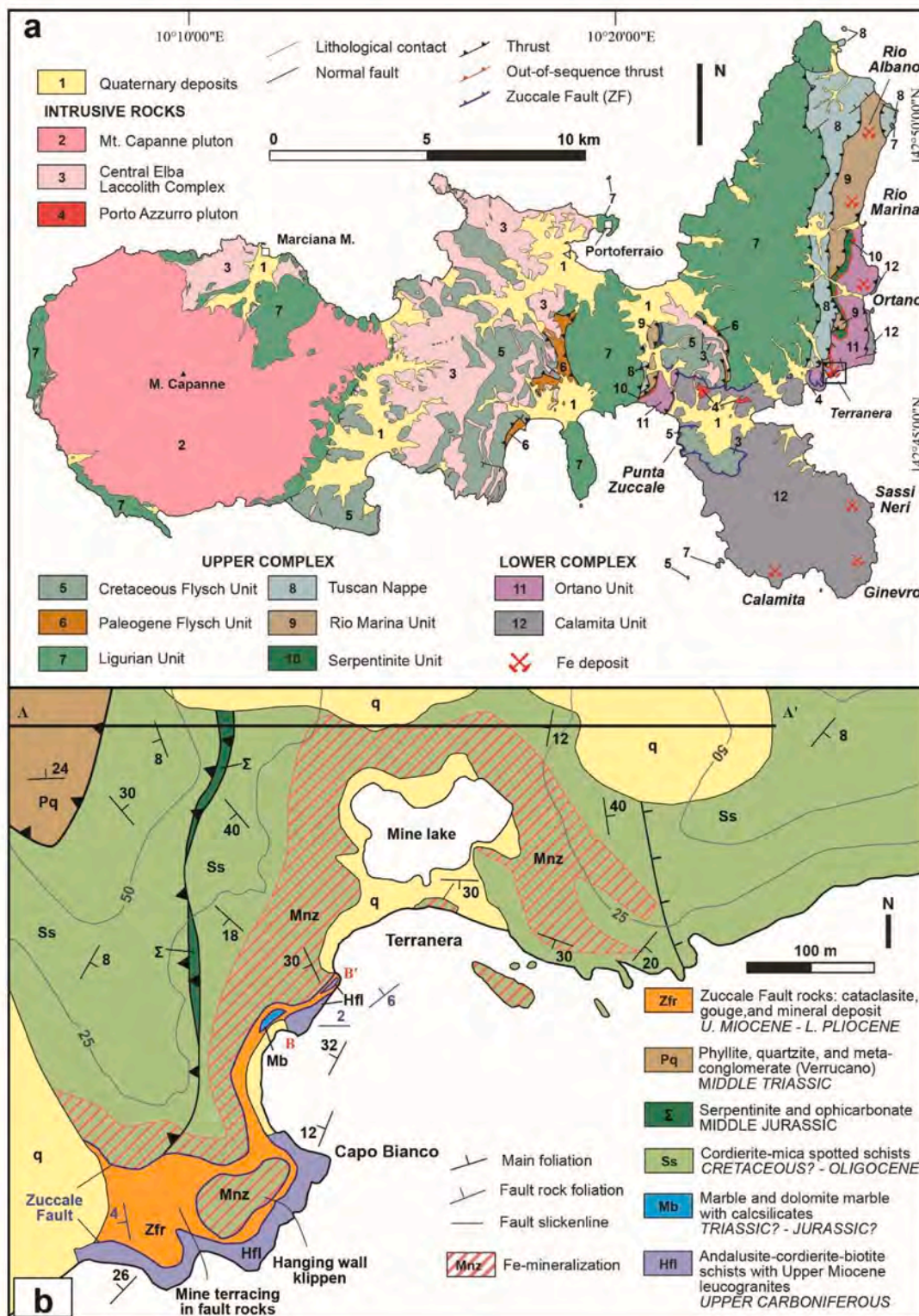

Fig. 1. Tectonic sketch of the Island of Elba (a) and geological map of the Terranera deposit (b). Modified from: Papeschi et al. (2021). The AA' trace of panel b locates the geological cross section of Fig. A1. The BB' segment marks the mapped area of the Zuccale fault that is studied in detail here (Fig. 2).

element imaging constructed using Laser Ablation-Inductively Coupled Plasma-Time of Flight Mass Spectrometry to constrain the fluid-rock interaction processes occurring within a fault that hosts a Fe-skarn mineralization. The studied case is the Zuccale fault of the Island of Elba (Italy), an upper crustal structure of the Northern Apennines that hosts an historical Fe-skarn deposit (Terranera) of the Elba ore district. We show that this dataset allows to define the key steps of skarn formation within the fault and suggests an ore environment that is transitional between skarn and epithermal. A comparison with other deposits from Elba and from a neighboring ore district of the Northern Apennines (pyritic ore district of south Tuscany) indicates that this environment could have been active in a region of the Apennines that extends well beyond the Island of Elba.

2. Geological overview

2.1. Regional geological setting

The Island of Elba of the Northern Apennine fold-and-thrust belt is a key region to study the relations between magmatic events, tectonic structures, and ore forming processes. In this island, thrusting and folding coupled with metamorphism from subduction to collision (Ryan et al., 2021). They were followed by shallow (<2GPa) late-Miocene intrusive magmatism (Poli and Peccerillo, 2016) and hydrothermal activity that led to the formation of several Fe deposits (Tanelli et al., 2001).

The nappe pile (Fig. 1a) dips to the W and verges to the E, and originated from the Cretaceous – Eocene oceanic subduction and the subsequent Oligocene – Miocene continental collision involving the Adria microplate and the European margin (Keller and Coward, 1996; Keller and Pialli, 1990; Papeschi et al., 2021; Pertusati et al., 1993). The uppermost, ocean-derived nappes (Fig. 1a) consist of two Flysch units of the Ligurian Unit, which rest on top of a stack of continent-derived nappes. The ocean-derived nappes cover most of the island, while the continent-derived nappes crop out mainly in eastern Elba (Massa et al., 2016), where the Fe deposits occur. From top to bottom, the continental units consist of the anchizone-facies Tuscan Nappe, the lower greenschist-facies Rio Marina Unit, and the amphibolite facies Ortano and Calamita Units. The Terranera Fe deposit is hosted by the Zuccale Fault (see below, Fig. 1b).

The shallow intrusions form a complex association of mantle-derived and crustal anatectic rocks (Dini et al., 2002; Musumeci and Vaselli, 2012; Papeschi et al., 2019; Poli and Peccerillo, 2016; Rossetti et al., 2008). These are the Monte Capanne granodiorite and the Porto Azzurro monzogranite intrusions (Fig. 1a). The Porto Azzurro Pluton of east Elba emplaced within the Calamita Unit at the base of the nappe stack (at c. 0.2 GPa pressure) together with a set of leucogranite dikes and veins between 6.53 and 5.9 Ma (Gagnevin et al., 2011; Maineri et al., 2003; Musumeci et al., 2015; Spiess et al., 2021). This was considered the causative pluton of the Fe deposits (Dünkel et al., 2003).

Gravimetric maps and borehole data show that the roof the Porto Azzurro monzogranite lies at a depth of c. 150–200 m below the sea level (Montecatini SpA, 1951; Musumeci and Vaselli, 2012; Papeschi et al., 2017), but its geometry, composition, and volume are unknown. A relatively large volume was postulated based on the evidence for a c. 60 km^2 contact aureole developed within the Calamita and Ortano units (Marinelli, 1959). The contact aureole was dated between 6.76 and 6.23 Ma based on Ar/Ar radiometric data on muscovite and phlogopite (Musumeci et al., 2015; Musumeci et al., 2011).

2.2. The Zuccale Fault

The Zuccale Fault (ZF) is an east dipping, top-to-the-east, low-angle (<10°) brittle fault that outcrops in eastern Elba and crosscuts the entire nappe stack including the Calamita Unit and the Porto Azzurro pluton (Fig. 1b). Its eastward horizontal displacement was estimated at about 6 km (Keller and Pialli, 1990). Due to its relevance for the regional tectonic evolution and fault-forming processes, the ZF is one of the most studied faults of the Northern Apennines (Collettini and Holdsworth, 2004; Keller and Coward, 1996; Musumeci et al., 2015; Pertusati et al., 1993; Smith et al., 2011; Viola et al., 2018).

The most documented section of the ZF is the one of Punta Zuccale (Fig. 1a) where the fault consists mainly of 1.5–3 m-thick matrix-supported breccias, as well as foliated and massive cataclasites (Keller and Coward, 1996; Musumeci et al., 2015; Viola et al., 2018) and sulfide-bearing cataclasites (Gundlach-Graham et al., 2018). Based on field relationships, Ar-Ar dating of the Porto Azzurro monzogranite, on Ar-Ar and U-Pb dating of hornfels from the metamorphic aureole and from the footwall block, and on K–Ar dates of fault gouges, several authors (Musumeci et al., 2015; Viola et al., 2022; Viola et al., 2018) proposed that the ZF started as a thrust at c. 22 Ma (late Miocene) but became selectively reactivated by out-of-sequence thrusts at <5 Ma due to the progressive structuring of the Northern Apennine orogenic wedge. The younger age identifies the brittle stage of fault activity during which the ZF displaced the thermal aureole of the Porto Azzurro Pluton after the peak metamorphic conditions. During this stage, the fault zone incorporated lenses of mylonitic dolomite marble that originally formed in reverse shear zones within the aureole (Musumeci et al., 2015). These lenses contain alternations of mm-thick phlogopite-diopside-tremolite phyllonites and calcite-dolomite levels (Fig. 2). One such blocks is shown in Figs. A0-A1 (Appendix).

3. Terranera and the Fe deposits of Elba

Ore exploitation at Elba and in the neighboring areas of Tuscany started at the dawn of civilization. At Elba and in the ancient harbor of Populonia of the mainland, iron mining, trading, and smelting can be traced back to the mid-6th century BCE, i.e. well before the Roman civilization (Becker et al., 2019). Iron was produced by 7 mines, which were exploited at different times, i.e. Rio Albano, Rio Marina, Ortano, Terranera, Calamita, Ginevro, and Sassi Neri (Fig. 1b, see also Appendix and Table A1). Mining in the district ended officially in 1981 (Tanelli et al., 2001).

Sparse geochronological and geochemical data hindered the development of a metallogenic model for eastern Elba. Six hematite and adularia samples from Rio Marina dated with the (U-Th)/He isotopic method gave ages between 5.36 ± 0.33 and 5.64 ± 0.11 Ma and between 5.575 ± 0.008 and 5.583 ± 0.013 Ma, respectively (Wu et al., 2019). These dates are undistinguishable from the 5.39 ± 0.46 Ma determined previously for the Rio Marina hematite with the same method (Lippolt et al., 1995).

The Terranera deposit (Fig. 1b) was the smallest of the district. It included two open pits (Terranera and Capo Bianco, Fig. 1b) and two galleries. Its historical production in the 1894–1943 period was of c. 311,000 t at a grade of 45–57 wt% Fe (Report, 1944). The ore bodies were described as a 10–30 m thick "heterogeneous friction breccia" (Fig. A2) and reported as lenses and veins of hematite, limonite, and pyrite embedded within cataclasites (Montecatini SpA, 1951). Pyrrhotite was reported in the deepest section of the deposit and lenses were hosted also by the rocks of the hanging wall block. They are still partly visible in the field today (Fig. 1b). West of Terranera, drill hole data showed evidence for the ZF crosscutting the Porto Azzurro pluton. East of Terranera, both fault and ore bodies were dissected by a set of normal faults, which juxtapose footwall and hanging wall. East of Terranera, the Spotted Schists hosted a magnetite-hematite-pyrite ore body (Fig. 1b), which made an integral part of the deposit.

4. Materials and methods

Fieldwork at Terranera was conducted to document geometry and lithology of the mineralized fault rocks (Fig. 2), identify the mineral paragenesis and select appropriate samples for a fluid inclusion study.
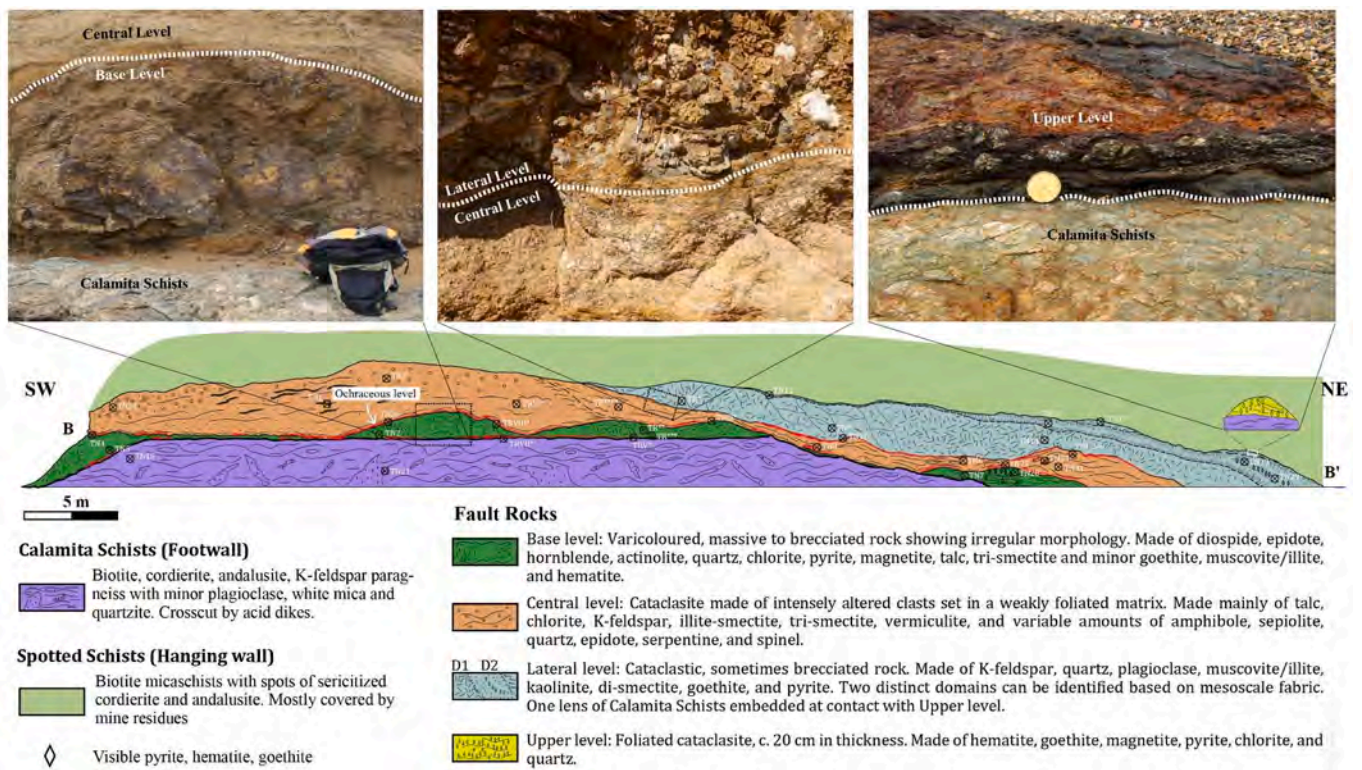
Fig. 2. Reconstruction and lithologies of the Zuccale fault at Terranera based on field and mineralogical documentation (cf. Fig. 1). In this outcrop most of the hanging wall is covered by mine residues. The small insert is added to highlight the Upper level of the fault. Symbols and associated names mark the 34 samples collected in this outcrop.

Forty-six samples were collected from the fault zone and from the protolith rocks at the footwall and hanging wall blocks, which were used for the subsequent multi-analytical documentation. Thirty-two of these samples are from the 70 m-long outcrop of the fault zone (Fig. 2), where the mineralized fault rocks can be documented in detail. Other 12 samples were collected away from this outcrop in order to capture as much as possible the *meso-* and microtextural features of Fe ore, footwall and hanging wall (e.g., Fig. A1).

The gathered dataset consists of field data, microtextural data, electron probe microanalyses (EPMA) of fault and protolith minerals, X-ray Powder Diffraction (XRPD) analysis of phyllosilicates, fluid inclusion microthermometric data, and elemental imaging of ore samples by Laser Ablation-Inductively Coupled Plasma - Time of Flight Mass Spectrometry (LA-ICP-TOFMS). We determined the element distribution maps of two samples from the Base level, which gave very similar results.

A detailed account on all the analytical techniques and on limits of detection, accuracy, and precision is given in the Appendix, which reports a representative list of analyses (Tables A2-A8). Here, we highlight that, due to the widespread evidence for mineral replacement textures, the petrographic study was carried out adopting the mineral association concept (Einaudi et al., 2003; Hedenquist and Arribas, 2022). This is a group of minerals that are characteristic of a given volume of rock, which are not in contact with each other and did not form necessarily all at equilibrium. Thus, the association phlogopite, talc, chlorite, quartz, muscovite/illite, magnetite, and hematite make the Base and Central levels, but the assemblages are actually chlorite + quartz and talc + tremolite + hematite (see below).

5. Fault rocks and ore body of Terranera

5.1. Field Data

At Terranera, the mineralized ZF shows an intense alteration of both

fault rocks and adjacent host rocks, which obliterate the pristine fabrics. The best exposure of fault rocks and mineralization is a NNE-SSW section, which is about 70 m long and represents the westernmost segment of the deposit (B-Ḃ of Fig. 1b). Based on rock fabric and mineralogical/petrographic characteristics, the mineralized fault rocks can be divided into 4 lithotypes that we call Base, Central, Lateral, and Upper levels, each one with its own specific fabric and mineral paragenesis (Fig. 2). These terms are purely geometrical and do not imply an interpretation of the structural architecture of the fault zone. The entire studied fault section is subhorizontal and its rocks are sandwiched between the high-grade Calamita Schists of the footwall and the muscovite-biotite-cordierite Spotted Schists of the hanging wall.

The Calamita Schists is a grey hornfels made of alternating light-colored, quartz-feldspar domains and dark greenish andalusite-cordierite-biotite schistose domains (Fig. 2). Late Miocene, quartz-feldspar-tourmaline dikes crosscut the metamorphic foliation of this rock. At the outcrop scale, the Calamita Schists do not show evidence for hydrothermal alteration close to the fault.

The Base level greenish breccia is discontinuous to massive and shows in places an ochraceous color (Fig. 2). It has an irregular morphology, subhorizontal attitude and turns into a thin foliated cataclasite at its base. Its thickness varies between c. 20 cm and 1 m, and the contacts with footwall and Central level are marked by ochraceous goethite and magnetite levels. The greenish color is given by the relative abundance of epidote, hornblende, actinolite, diopside, and clay minerals. Fractures and discrete volumes of this rock host pyrite, goethite, magnetite, and hematite, which occur also at the contact with the footwall.

The Central level is a fine grained, poorly cohesive and weakly foliated cataclasite whose thickness decreases substantially towards the NE (Fig. 2). It shows a maximum thickness of c. 3 m. The foliation is marked by some ochraceous/dark levels made of a clay mineral association, Fe oxides, and limonite. The matrix of this cataclasite is made of

several clay minerals (see below), and the clasts vary in size between few mm to 20 cm. Clast lithologies can hardly be recognized at the outcrop scale due to the intense argillic alteration. Their size decreases progressively towards the contact with the Base level.

The Lateral level is a heterogeneous, hydrothermally altered rock made of two distinct domains (Fig. 2). The first one (D1) is a poorly cohesive, whitish rock made mainly of a fine-grained matrix. Its main characteristics are the lack of visible clasts, apparently massive texture, and the presence of continuous stringers made of clay minerals and limonite and with a thickness of up to several cm. The morphology of D1 is lenticular and its maximum thickness is c. 2 m. Domain 2 (D2) is a massive level made of a goethite-clay mineral assemblage. Goethite is disseminated for a thickness of c. 1 m and provides an effective cementation to this rock. It gives a distinct ochraceous color that is well visible in the field. Goethite occurs as coarse euhedral crystals (up to 1 cm in size) or within stringers of undeformed, mode-I quartz veins.

The 15–20 cm thick Upper level is a foliated cataclasite in which large pyrite crystals (up to 1 cm in size) are set in a penetrative foliation made of hematite, goethite, limonite, chlorite, and quartz (Fig. 2). The Fe-oxides are also coarse-grained, and the pyrite is visibly fractured. This level is in contact with a lens of Calamita Schists embedded within D2.

The Spotted Schists of the hanging wall is made of fine-grained, grey/greenish schists that were intensely altered and lost their pristine fabric. This rock shows, however, typical features at the microscopic scale.

5.2. Microtextural data

The Calamita Schists of the footwall show levels of lepidoblastic biotite alternating with levels of granoblastic quartz and K-feldspar. Minor andalusite, plagioclase, tourmaline, and ilmenite occur at the contact between lepidoblastic and granoblastic levels (Fig. 3a). Close to the fault contact, the schists are crosscut by thin veins hosting euhedral phlogopite, quartz, goethite (Fig. 3b).

The hanging wall Spotted Schists are made of quartz porphyroclasts set in an intensely foliated vermiculite matrix (Fig. 3c). Mode-I quartz-hematite veins crosscut this rock. Away from the ZF, the rock is made of clinozoisite- and phlogopite-rich clasts replaced by clay minerals. Other lithologies are a breccia in which euhedral and zoned goethite is set in a phlogopite, muscovite, chlorite, vermiculite matrix, and a breccia in which chlorite-vermiculite and phlogopite clasts are set in a goethite matrix (Fig. 3d).

The Base level shows consistently a texture made of massive bands of early clinozoisite and diopside, which are replaced by Fe-rich pleochroic hornblende (Fig. 4a) and quartz. Hornblende itself is replaced by fine-grained actinolite showing intense reddish pleochroism and texturally coeval talc, chlorite, and sericite. Massive hematite is embedded within amphibole, talc, illite, and 1-water layer tri-octahedral smectite. Locally, later replacement by smectite obliterates this microtexture making phase identification difficult. Another key feature is the abundant pyrite, which occurs as subhedral, intensely fractured crystals that are replaced by goethite. In one sample, euhedral bulky magnetite is associated with euhedral lamellar talc (Fig. 4b) but is cut by extensional goethite veins.

The Central level cataclasite is the mineralogically and texturally most heterogeneous fault rock. Its matrix consists of a mineral association including anhedral and fractured clinozoisite, Mg-rich spinel, K-feldspar, diopside, phlogopite, clinochlore, talc, illite, and quartz that are replaced by several clay minerals (2-water layers tri-octahedral smectite, vermiculite, sepiolite, serpentine, interstratified illite–smectite, see below). An ochraceous, Fe-Mn-rich phase and minor titanite, zircon, and rutile are also present. These minerals occur systematically as relicts that replace each other or that are replaced by the
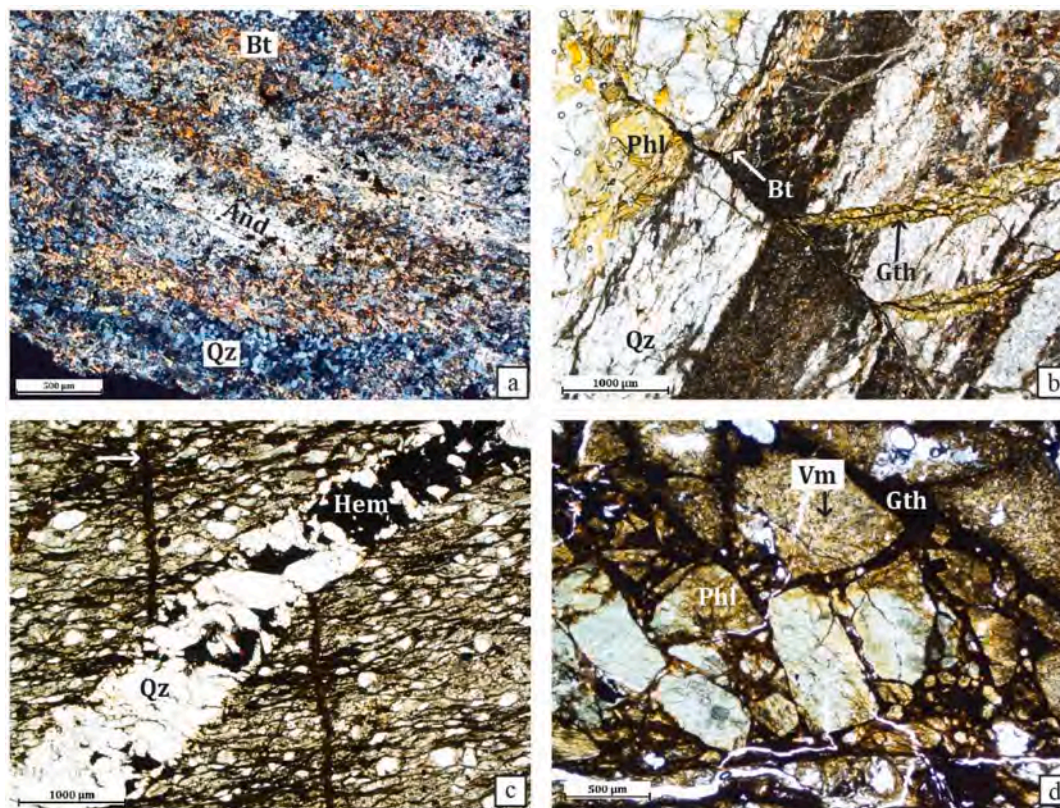

Fig. 3. Textural features of the footwall Calamita Schists (a, b) and hanging wall Spotted Schists (c, d) of Terranera. a. TN15: lepidoblastic biotite levels alternating with anhedral andalusite. b. TN15: quartz and biotite levels crosscut by a set of thin phlogopite, quartz, and goethite veins. c. TN16: foliated fabric of Spotted Schists crosscut by an extensional quartz-hematite veinlet. d. TN32: matrix supported breccia in which fractured, vermiculite-phlogopite clasts are set in a goethite matrix. Mineral abbreviations in this and other figures follow Whitney and Evans (2010).
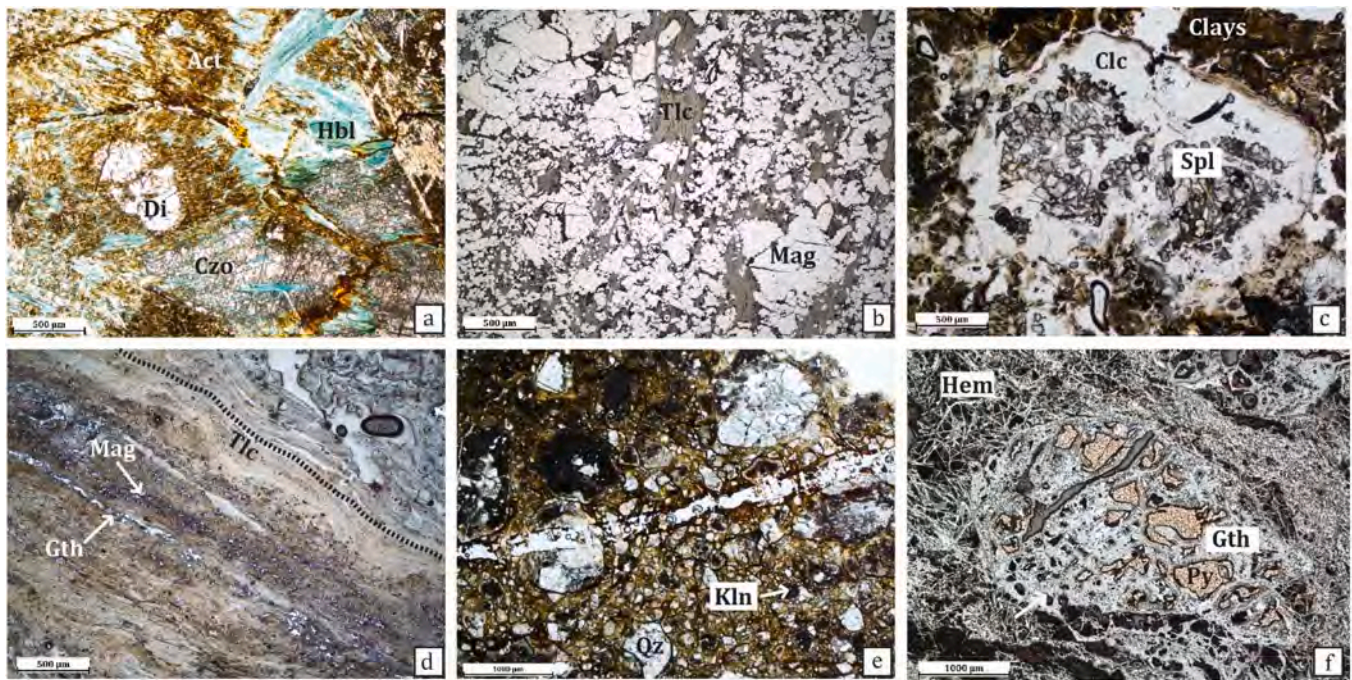
Fig. 4. Typical textures of the Zuccale fault at Terranera. a. Base level (TRII). Anhedral and fractured diopside associated with hornblende and subhedral and fractured clinozoisite. Hornblende is replaced by actinolite along the cleavage plains. b. Base level (AC6). Subhedral magnetite set in a talc matrix (reflected light, parallel nicols). c. Central level (TRVI). Relict, fractured spinel replaced by clinochlore and set in a clay-rich matrix. d. Central level (TRVIII). Matrix foliation marked by alternations of talc bands and magnetite-goethite bands (reflected light, parallel nicols). e. Lateral Level (TN14, D1). Quartz-feldspar clasts set in abundant kaolinite and muscovite-illite matrix. The core of the feldspar clasts are altered by kaolinite. f. Upper level (TNX26). Relict pyrite crystal replaced by goethite and embedded within massive boxwork hematite (reflected light, parallel nicols).

late clay minerals (Fig. 4c). Talc is one of the most abundant minerals of this rock and is observed as an aggregate of isooriented crystals forming the foliation of the rock and embedding magnetite and goethite (Fig. 4d). Magnetite, hematite, and pyrite are often associated, but the latter is volumetrically minor and always relict. Goethite is always found to replace pyrite and Fe-oxides. Euhedral hematite is sometimes found within magnetite (martitization). Intensely fractured and relict K-feldspar clasts are typically found within this cataclasite. They show intense replacement of K-feldspar by illite, phlogopite, chlorite, and clay minerals.

In the Lateral level, Domain 1 consists of rounded quartz-K-feldspar clasts set in a matrix made of kaolinite and illite (Fig. 4e). The K-feldspar is typically replaced by kaolinite and the whole rock is crosscut by thin, mode-I veins made of quartz and clay minerals. Domain 2 is a more competent rock because of the relatively minor abundance of clay-rich matrix and replacement textures. The rock is made of flattened and isooriented quartz-phlogopite clasts associated with minor, biotite, and plagioclase. Pyrite and goethite are commonly present, but pyrite is systematically replaced by goethite.

The Upper level is made of isooriented, lamellar hematite forming a boxwork texture (Fig. 4f) set within quartz, chlorite, magnetite, pyrite, goethite, and rare chalcopyrite. Pyrite is systematically replaced by goethite, while minor subhedral and fractured magnetite is present as relict. Chlorite is subhedral-euhedral and aligned along the foliation.

A summary of the paragenetic reconstructions of the fault rocks is given in Fig. 5.

5.3. X-ray diffraction data

The Base, Central, and Lateral levels show complex associations of phyllosilicates that vary as a function of lithology (Table 1). In the Base and Central level samples, the combination of air-dried and ethylene glycol solvated XRD patterns shows an association of talc, chlorite, illite, interstratified illite–smectite (Fig. 6acd), and 1-water layer tri-octahedral smectite (Fig. A3acd). These phases occur together with vermiculite, sepiolite, serpentine, and 2-water layers tri-octahedral smectite, which are present at variable proportions. The Lateral level is characterized by the presence of kaolinite in addition to muscovite/illite (Fig. 6b) and 1-water layer di-octahedral smectite (Fig. A3b).

5.4. Mineral chemistry data

The EPMA of epidote and diopside from the Central and Lateral levels show relatively consistent compositions (Table A2), which do not vary irrespective of the modal abundance of these minerals and of their euhedral or relict morphologies. In contrast, the amphiboles from the Base and Central levels show compositions that are clearly distinct. The Base level hosts Fe-rich amphiboles having $Mg/(Mg + Fe)$ always < 0.5 (Fig. 7b), while the clasts of the Central level hosts Mg-rich amphiboles with $Mg/(Mg + Fe) > 0.5$ (tremolite, Mg-hornblende).

The tri-octahedral micas from the Central level are those with the highest Mg concentrations of the entire dataset and correspond to phlogopite compositions (Fig. 7a, $Fe/(Fe + Mg) < 0.3$), while those of the Lateral level show more variable compositions in which $0.6 > Fe/(Fe + Mg) > 0.3$. These compositions are very similar to those of the Calamita and Spotted Schists (Fig. 7). The composition of the Mg spinel from the Central level (Table A7) approaches the stoichiometric formula ($Mg_{0.97}Al_{2.01}O_4$). Similarly, the di-octahedral micas from the Central level show the highest Mg concentrations (Table A6) and have compositions corresponding to that of muscovite/illite. In contrast, the muscovite from the quartz pressure shadows of the Spotted Schists shows a $Fe/(Fe + Mg) > 0.5$ (Fe-celadonite end-member: c. 6 %).

Talc from the Central level (Table A6) has a quite homogeneous composition, as well as the K-feldspar from the Central and Lateral levels (albite proportion always < 6 %).

Chlorite from the Central and Upper levels (Table A4) has compositions that approach that of the clinochlore end-member, and has systematically a $Mg/(Mg + Fe) > 0.8$. Notably, this Mg-rich chlorite is the
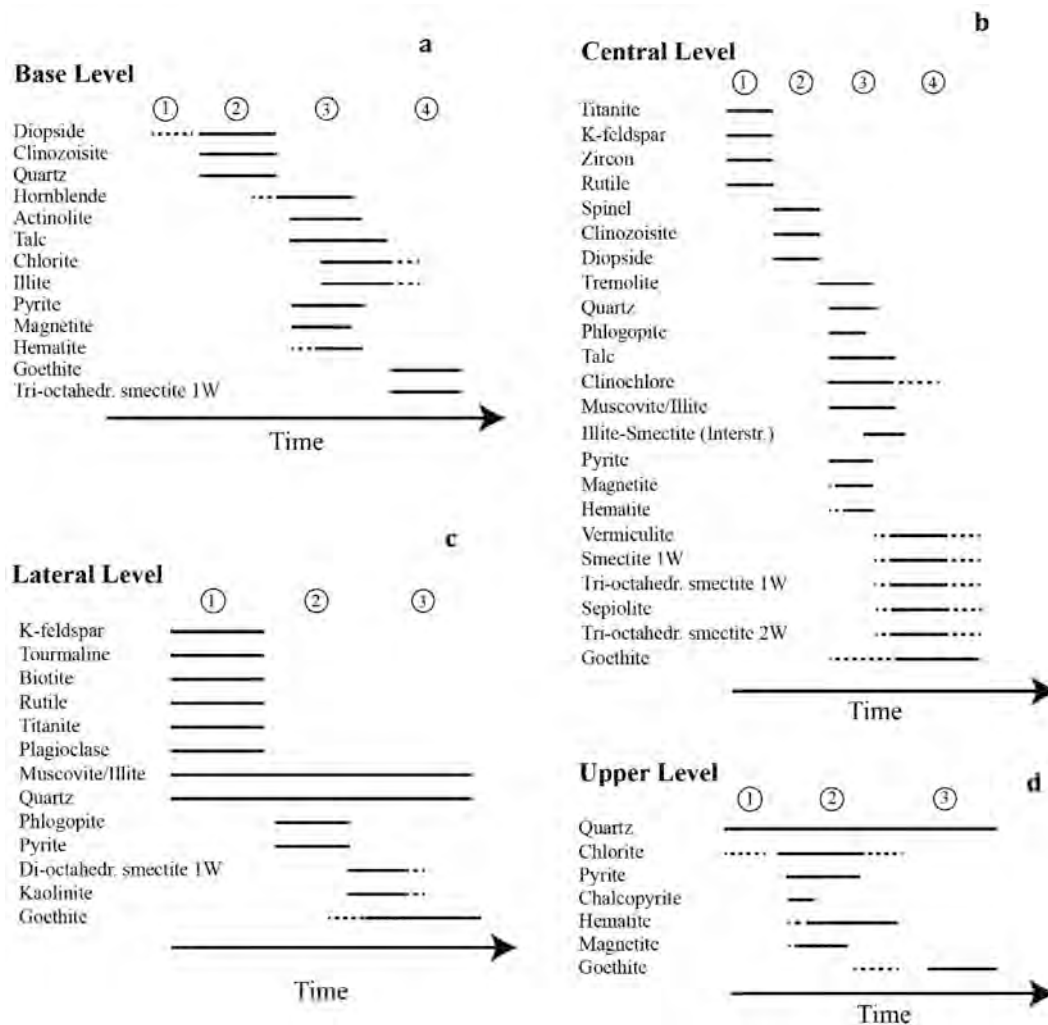
Fig. 5. Mineral paragenesis of the Zuccale fault at Terranera.

Table 1

Phyllosilicates the Zuccale Fault of Terranera as determined by XRPD analyses.

Fault rock/ protolith	Samples	Mineral association
Base level	TN2; TN28; TN40; AC6	Talc; chlorite; muscovite/illite; tri-smectite 1W
Central level	TN1; TN3; TN10; TN20; TN31; AC4	Chlorite; talc; tri-smectite 2W; vermiculite; muscovite/illite; sepiolite; serpentine; illite–smectite
Lateral level	TN14 (D1); TN17 (D2); TN29 (D2); TN30 (D2)	Muscovite/illite; kaolinite; di-smectite 1W
Spotted Schists	TN16; TN32; TN33	Muscovite/illite; vermiculite; chlorite-smectite (corrensite)
Calamita Schists	TN15	Illite; kaolinite
Carbonatic cataclasite*	TN23	Chlorite; muscovite/illite; pyrophyllite; smectite-1W
Eastern ore body	TN35	Talc

Notes: the mineral associations focus on clay minerals and chlorite and is reported as a function of determined abundance in the samples. Muscovite and illite are reported together due to difficulty to discriminate them based only on XRD data. Smectite-1W: 1 water layer smectite. Smectite-2W: 2 water layers smectite. *: see Fig. A1 of Appendix.

one associated with quartz and replacing the Al-Mg spinel of the Base Level (Fig. 4c) and is also associated with illite, phlogopite, and clay minerals in replacing the clasts of the Central level.

Hematite from the Upper level shows FeO mass fractions > 90 wt% (Table A8). The only minor components that were determined at higher concentrations with EPMA have been Al_2O_3 (0.87–1.15 wt%) and SiO_2 (0.17–0.51 wt%), while other minor/trace components including CaO, MnO, and TiO_2 show mass fractions < 0.1 wt%.

Laser Ablation-ICP-TOF element imaging of two samples from the Base level shows several compositional and textural features that integrate substantially the petrographic study and the EPMA of the fault minerals. These features are shown in Fig. 8, which shows a selection of element distribution images of a Basel level sample (AC6) in which hematite occurs with amphibole, talc, illite, and tri-smectite 1W. The data show that only a relatively small number of mostly lithophile, minor/trace elements are hosted by the phyllosilicates, namely Ca, Al, Mn, Na, Cu, Zn, Sr, Co, Y, Sc, and Zr (see also Fig. A3 of the Appendix). These elements show concentrations ranging between 1.5 wt% and 5 μg/g and are irregularly distributed. The distribution maps reveal that their concentrations vary at the scale of few tens of μm, marking the positions of distinct phyllosilicate crystals along the foliation of the cataclasite.

Hematite contains mostly siderophile and chalcophile trace elements, which define peculiar textural and compositional characteristics. Tin shows concentrations of c. 5 wt%, while W is present at c. 2000 μg/g (Fig. A3). Gallium, Ge, and V are present at mass fractions between 50
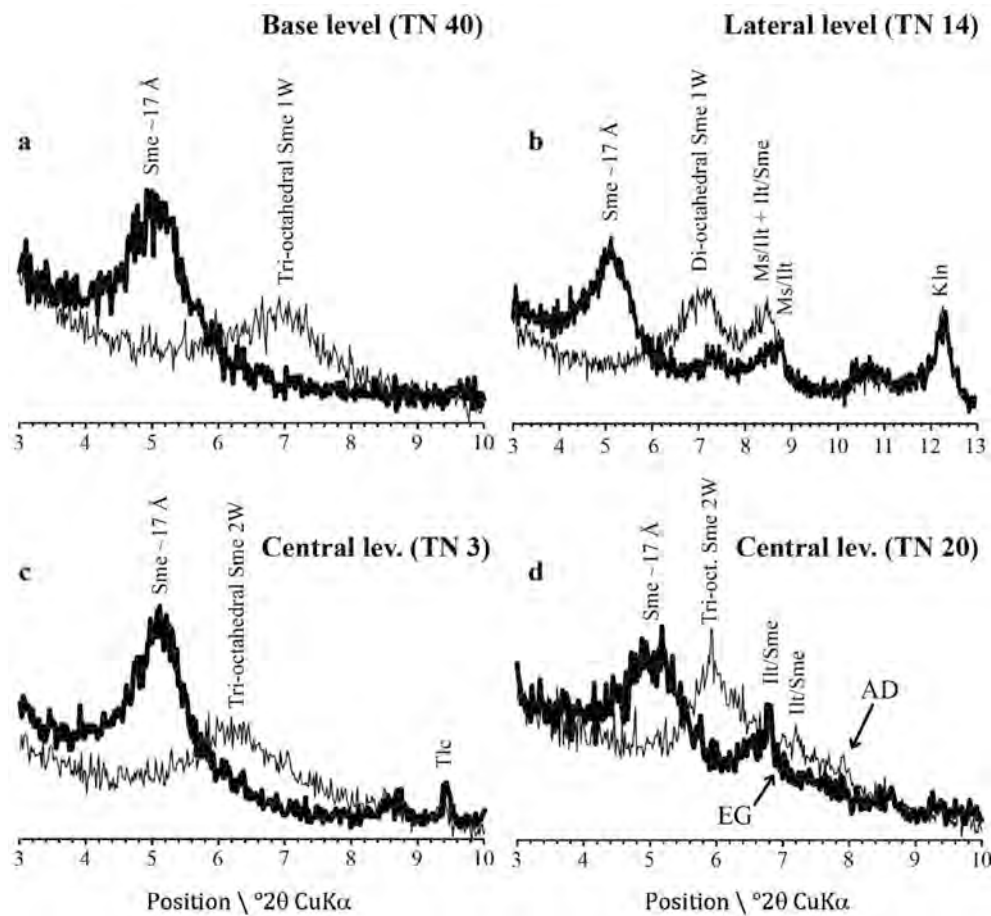
Fig. 6. Representative XRPD patterns of clay minerals from the Base, Central and Lateral levels (see also Table 1). Each panel shows air-dried (AD) and ethylene glycol solvated (EG) analyses of the same sample.

and 200 µg (Fig. 8). A large number of elements including Ti, As, Y, Mo, Te, REEs show mass fractions ranging between about 50 and 1 µg/g. Interestingly, Ti, V, Ge, Ga, and Sb show a zoned distribution within hematite, revealing that this phase crystallized in an open space within the cataclasite. Because of their relevance for the genetic model of mineralization, we highlight in particular the element suite Sb, Ga, Ge, and As.

5.5. Fluid inclusion data

Three samples from undeformed mm-thick, quartz-goethite extensional veins were selected for a fluid inclusion study. These samples were collected close to the contact between Base and Central levels, along the NE-dipping cataclastic foliation (Fig. 2). The veins show a comb texture (Fig. 9a). Eight fluid inclusion assemblages (FIAs) were studied from these veins. They are all hosted by euhedral quartz, which occur together with euhedral-subhedral goethite, hematite, magnetite, and clays. One distinct feature of all these FIAs is that the host quartz of the mode-I veins shows little crystalline deformation. The FIAs are mostly secondary (Fig. 9b) and pseudosecondary (Fig. 9c) with respect to quartz crystallization, showing that the fault fluid was entrapped during and after quartz crystallization. At laboratory temperature, the entrapped fluid is invariably-two-phase (liquid–vapour) and with a degree of filling of the vapour of c. 25–30 vol%.

The microthermometric measurements show several phase transitions that include the T of eutectic melting (Te), the T of hydrohalite melting (Tmhh), the T of ice melting (Tmice), and the total homogenization T (Thtot), most of which are very consistent in each assemblage (Table 2). However, the range of Te values is comprised between c.

-22 °C and -75 °C, which shows evidence for significantly different fluid compositions in the 8 FIAs. Values of Te comprised between -21 and c. -30 °C can be considered an indication of a fluid dominated by monovalent cations (Goldstein and Reynolds, 1994), while values as low as -75 °C indicate much more complex fluid compositions that include the species NaCl, KCl, $CaCl_2$, $MgCl_2$, $FeCl_2$, $FeCl_3$ for which no equation of state is available (Steele-MacInnis et al., 2016). These very low Tes complicate the identification of the ore fluid composition, and considering that some of them may also result from metastable eutectic melting in high-salinity inclusions (Goldstein and Reynolds, 1994), they generate a variable degree of uncertainty in the definition of fluid composition. Hence, while the properties of FIA 2, 4, and 5 can be approximated by those of the H_2O-NaCl model fluid, those of all other FIAs can be approximated by the H_2O-NaCl-$CaCl_2$ model fluid (Table 2) with the proviso that such fluid does not allow the precise determination of the ore fluid properties. Considering the range of measured Tmhh and Tmice (Table 2), the estimated mass fractions of NaCl in FIAs 2, 4, and 5 range between about 1.6 and 13.4 mass%. The mass fractions of NaCl and $CaCl_2$ in FIAs 1, 3, and 6–8 is 4.5–16.4 and 10–21.1 mass%, respectably.

The high temperature determinations of FIAs 1–8 show consistent ranges of Thtot in the entire dataset, as all FIAs homogenized by bubble disappearance between 320 and 325 °C (FIAs 1, 2, 3, 5, 6, 9) and between 260 and 285 °C (FIAs 4 and 8).
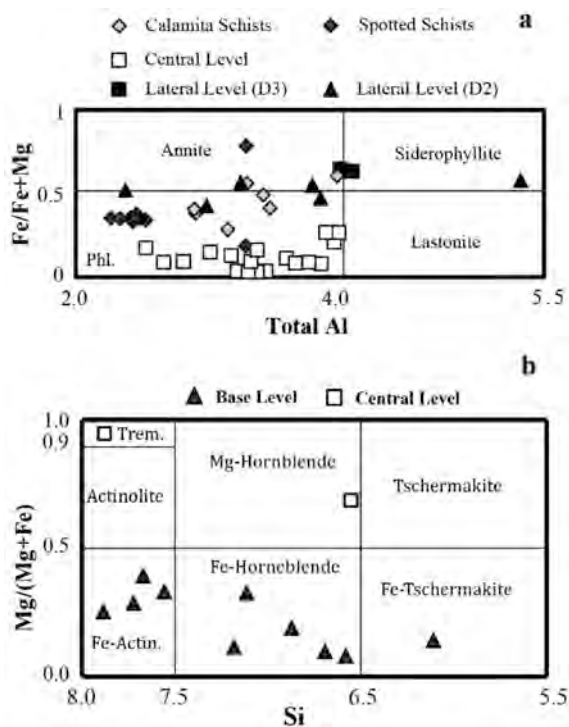
Fig. 7. Composition of representative hydrothermal minerals in fault rocks and protolith. a. Classification scheme of dark micas (from: Pieczka et al., 2013). b. Classification scheme of amphiboles (from: Leake et al., 2018).
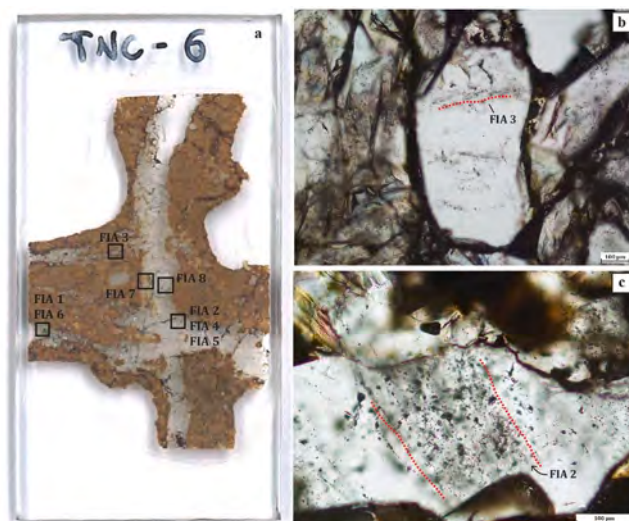

Fig. 9. Typical textures of the FIAs hosted by the Zuccale fault at Terranera, and relations with mode I veins. a. Doubly polished thin section containing quartz-goethite-magnetite-hematite veinlets that occur within the Central level close to the contact with the Lateral level (TNC-6). The black squares locate the positions of the studies FIAs. b. Secondary FIA 3 within euhedral quartz. c. Pseudosecondary FIA 2 made of the coalescence of microfractures that cut orthogonally a quartz prism associated with clay minerals.
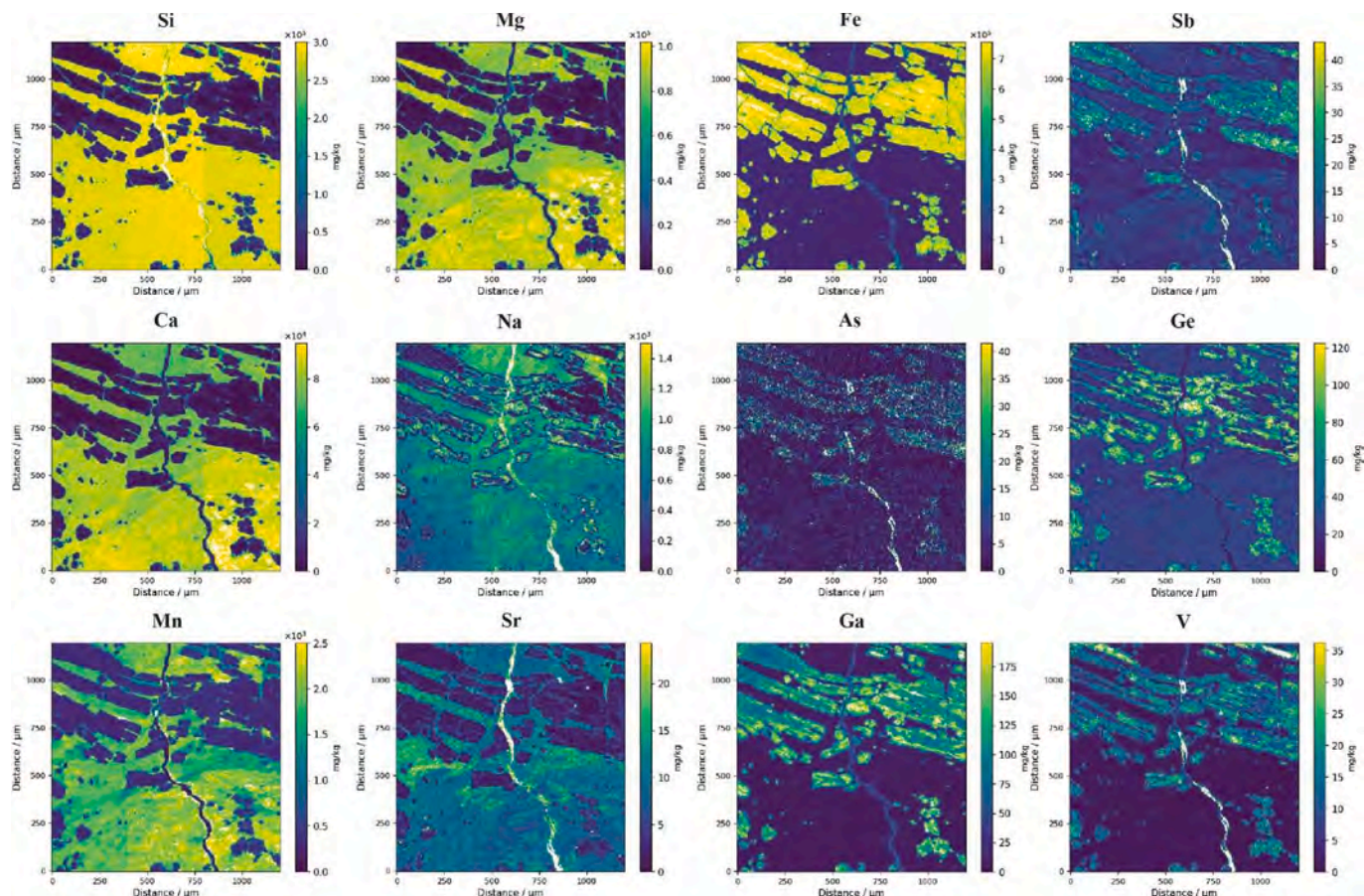

Fig. 8. Laser Ablation-ICP-TOFMS elemental images of a selection of major-, minor-, and trace- components of a hematite-phyllosilicate sample from the Base level.

Table 2
Microthermometric data of fluid inclusion assemblages from the ZF at Terranera.

FIA	N	φ (%)	Phase State	Te	Tmhh	Tmice	Mass% NaCleq	Mass% NaCl	Mass% CaCl₂	Thtot	Hom. Mode
1	7	25	L-V	−26.0	−25	−10.3 ± 0.3		16.4	9.9	326 ± 3	L
2	11	25	L-V	−21.7		−0.9 ± 0.0	1.6			321 ± 17	L
3	16	25	L-V	−60.5	−35	−30 ± 0.0		4.5	21.1	323 ± 3	L
4	10	20	L-V	−24.5		−9.5 ± 0.0	13.4			263 ± 0	L
5	11	25	L-V	−24.5		−8.6 ± 0.2	12.4			323 ± 2	L
6	15	20	L-V	−30.0	−25.5	−20.5 ± 0.0		11.8	10.0	323 ± 0	L
8	10	20	L-V		−33	−23.6 ± 0.0		4.9	17.9	285 ± 2	L
9	30	25	L-V	−75.0	−34.6	−28.3 ± 0.0		4.5	20.4	319 ± 1	L

Notes: all temperatures in °C. N = number of measurements for each FIA. Te = eutectic temperature; Tmhh = temperature of hydrohalite melting; Tmice = temperature of ice melting. Thtot = temperature of total homogenization. Mass% NaCleq = bulk salinity of FIA calculated using phase transitions and the software package Fluids 1 of Bakker (2003). The concentrations of NaCl and CaCl₂ have been estimated using the H_2O–NaCl–CaCl₂ model fluid of Steele-MacInnis et al. (2011).

6. Discussion

6.1. Magnesian Fe skarn formation

In the Calamita Schists of the footwall, the association andalusite, quartz, K-feldspar, muscovite, ilmenite, and biotite (Fig. 3a) results from the late-Miocene thermo-metamorphic imprint of the Porto Azzurro intrusion (Musumeci and Vaselli, 2012). In contrast, the thin quartz, phlogopite, goethite, and pyrite veins crosscutting the schistosity (Fig. 3b) represent the product of later hydrothermal activity. These veins are the only evidence for hydrothermal alteration of the footwall, which suggests that only limited interaction between the fault fluid and footwall took place.

The paragenesis of the Base level cataclasite is made of early diopside, clinozoisite, and quartz that is replaced by hornblende, actinolite, talc, chlorite, illite, tri-octahedral smectite-1W, pyrite and magnetite (Figs. 4a, 5a). The evidence for magnetite and hematite forming together with talc and other Mg phyllosilicates (Figs. 4b and 8; Fig. A3) suggests oxidation of magnetite after its deposition. The Central level shows early diopside, clinozoisite, K-feldspar, and Mg-rich spinel (Fig. 4c) that are replaced by an association of magnetite- and hematite-bearing tremolite, phlogopite, talc, chlorite, muscovite/illite, and interstratified illite–smectite. The amphiboles and micas of the Central level are those with the highest documented Mg contents (Fig. 7).

We interpret these paragenetic and compositional characteristics as close to those reported in the literature for the magnesian Fe skarn deposits (Einaudi et al., 1981; Meinert et al., 2005). Accordingly, Terranera formed as a result of metasomatic transfer between a hydrothermal fluid infiltrating the fault and a dolomite-rich protolith that was present therein (e.g., Fig. A0-A1). Such lithology could be the Calanchiole marble Fm. (Musumeci and Vaselli, 2012), which outcrops within the ZF at Punta Zuccale (Musumeci et al., 2015) and that hosts other ore deposits of Elba (i.e., Ortano, Calamita. Table A1). We propose that the result of this interaction was the mineral association hornblende, actinolite, talc, clinochlore, phlogopite, muscovite/illite, and quartz of the Base and Central levels, which formed during a magnetite-hematite-bearing retrograde stage. The prograde skarn minerals were Mg-spinel, clinozoisite, and diopside. Notably, this interpretation is consistent with what was documented in two relevant examples of magnesian skarn deposits, i.e. the world-class (Fe-)Cu skarn of Ertsberg East, Java (Rubin and Kyle, 1998) and the Saheb Fe-skarn of Iran (Baghban et al., 2021). In these deposits, the ore-bearing retrograde stage took place at c. 300–440 °C at the expenses of a dolomitic protolith, the main ore minerals were magnetite (Saheb) and magnetite-bornite-chalcopyrite (lower skarn of Ertsberg East), and the retrograde mineral association was made of tremolite-actinolite, chlorite, talc, serpentine, and phlogopite.

The quartz, phlogopite, chlorite association of the Lateral level is consistent with a magnesian skarn ore environment, as well as the chlorite-quartz assemblage of the Upper level. Both fabric and mineral compositions of the Lateral level suggest a derivation from a metamorphic or igneous protolith. Possible candidates for such lithology are the leucogranitic dikes that crosscut the Calamita Schists of the footwall (Fig. 2), which are widespread in the mine area.

A specific characteristic of Terranera is the goethite-clay mineral association, which defines the final stages of ore precipitation within the fault (Fig. 4df; Fig. 5). During these stages, a pervasive replacement of pyrite by goethite and replacement of the skarn minerals by muscovite/illite and several clay minerals took place. As shown below, this alteration is an integral part of the skarn process.

6.2. Ore fluid constraints and mechanism of ore deposition

The chlorite-quartz geothermometer of Bourdelle and Cathelineau (2015) can be used to constrain the range of temperatures of the retrograde skarn stage (Fig. 10). This is based on the hypothesis that chlorite and quartz were in thermodynamic equilibrium at the time of formation. The composition of chlorite in contact with quartz from the Central and Upper levels indicates that this mineral pair formed between c. 350 and 180 °C. These are the temperatures at which clinochlore replaced the Mg-spinel in the Central level (points 1–4 and 6–7 of Fig. 10; Fig. 4c), chlorite-quartz formed with muscovite/illite and phlogopite (point 5), and chlorite-quartz formed in the Upper level (points 8–9).

The phase transitions documented for the eight FIAs (Fig. 11) provide constraints on the physical–chemical properties of the fault fluid at the time of hematite and magnetite precipitation (retrograde stage) within the mode-I quartz veinlets of the Central level. The systematic homogenization by bubble disappearance shows that the FIAs were in a homogeneous state at the time of entrapment. The ranges of calculated bulk salinities and Thtot define two distinct trends in the dataset (Fig. 11a), one showing a salinity decrease from 26.3 to 1.6 NaCl + CaCl₂ mass % at about 325 °C and another showing salinity decrease and cooling to 13.4 mass% NaCl + CaCl₂ and 260 °C, respectively.

We stress that the fluid properties described above are typical of magnesian Fe-skarn deposits. They are for instance similar to those of the Saheb deposit of Iran (Baghban et al., 2021), in which FIs entrapped within the retrograde-stage epidote and quartz, and paragenetically coeval with magnetite, pyrite, chalcopyrite, amphibole, serpentine, and talc show Thtot mostly in the 220–420 °C range and the salinity between c. 5 and 48 wt%NaCleq.

We interpret the extreme salinity variations at constant T of Terranera a product of *mixing* of fluid batches having distinct salinities but similar T within the fault. This mixing was coupled with *cooling*. These combined processes must have been extremely efficient in precipitating magnetite and hematite, as Fe and Cl form several stable aqueous complexes (e.g., $FeCl^+$; $FeCl_2$; $FeCl_2^+$) in high-temperature saline hydrothermal fluids (Stefansson et al., 2008; Testemale et al., 2009) and the concentration of these complexes must have been initially very high in the fluid. As the solubility of these Fe-chloride complexes in geofluids
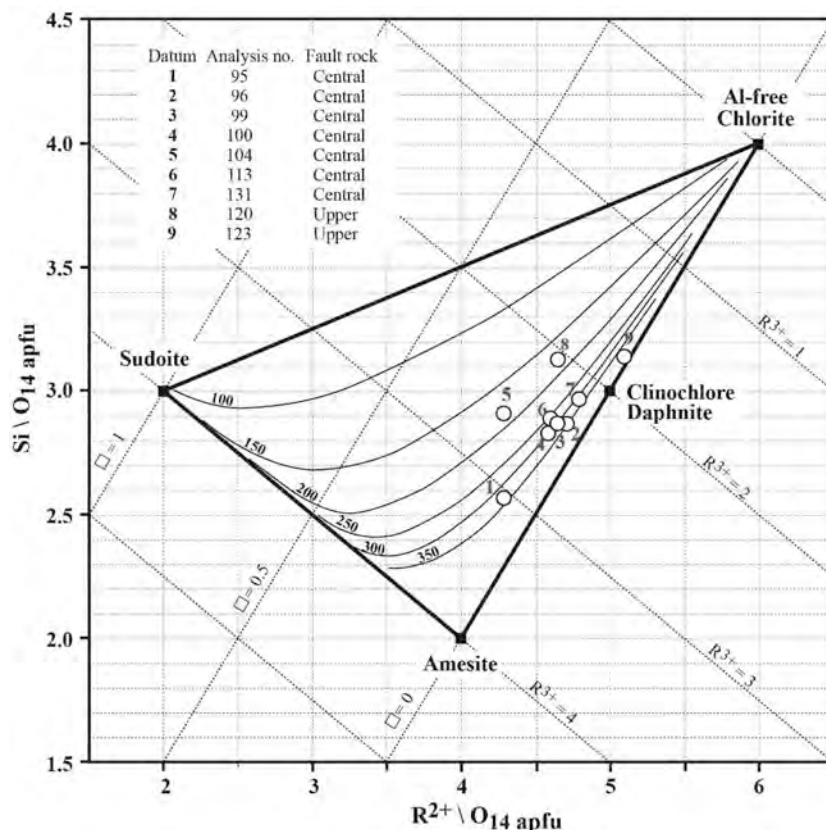
Fig. 10. Equilibrium formation temperatures of the chlorite-quartz assemblage from the Central and Upper levels of the Zuccale fault as estimated with the Bourdelle and Cathelineau (2015) geothermometer. See Table A4 (Appendix) for details on analyses.
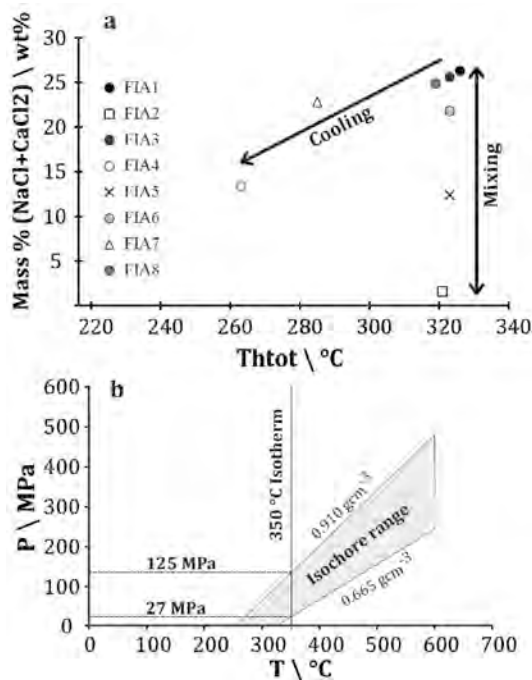

Fig. 11. Microthermometric and physical–chemical properties of the hydrothermal fluid of the Zuccale fault at Terranera. a. Thtot vs salinity trends. b. Range of calculated isochores for the 8 studied FIAs based on a model H_2O-$NaCl$-$CaCl_2$ fluid. The 350 °C isotherm is the maximum T of chlorite-quartz formation in the fault.

is prograde (Seward and Barnes, 1997), it is expected that a combination of efficient mixing and cooling caused effective precipitation of magnetite and hematite.

Clay mineral associations are distinct in the fault rocks of Terranera. In the Base and Central levels, goethite is mainly associated with tri-smectite-1W, tri-smectite-2W, vermiculite, illite/smectite, and sepiolite while it is preferentially associated with kaolinite and di-smectite-1W in the Lateral level. These associations are not typical of magnesian Fe-skarns (Baghban et al., 2021; Einaudi et al., 1981; Meinert et al., 2005); thus, they represent a specific characteristic of Terranera that warrants a detailed analysis. The first constraint provided by this association is represented by the goethite stability in hydrothermal fluids, which is defined at T < 200–250 °C by experimental data (Diakonov et al., 1994; Majzlan et al., 2003a; Majzlan et al., 2003b). This interval can be considered the upper stability limit of goethite-clay minerals in all fault lithologies of Terranera. A second constraint is given by the clay mineral association, which deserves special attention because its mineral composition, in combination with microtextural analysis and other geochemical data, may aid in the reconstruction of several ore environments (Hedenquist and Arribas, 2022). On this regard, a fundamental point to consider is that the clay minerals forming within ore bodies – e.g., kaolinite, dickite, illite, illite–smectite, pyrophyllite, and diaspore – may be associated with muscovite and sulfates (e.g., alunite, jarosite) to form classic "mineral groupings" (Hedenquist and Arribas, 2000). These are the mineral associations defined in the literature (Einaudi et al., 2003; Hedenquist and Arribas, 2022), whose precipitation conditions are controlled by T (range: c. 150–300 °C) and K^+/H^+ activity ratios of the hydrothermal fluid. Typical clay mineral associations form out of equilibrium because the T stabilities of the individual minerals do not overlap (Hedenquist and Arribas, 2022). However, they may define systematic and predictable changes of T and K^+/H^+, which pin down pathways of hydrolytic alteration in ore bodies. If such

pathways are identified, the clay mineral associations define specific types of hydrothermal alteration (i.e., high- vs low-sulfidation argillic alteration: Hedenquist and Arribas, 2022, and ref. therein). At Terranera, the 1-water layer smectite of the Base and Lateral levels (Fig. 6, Table 1) indicates a formation T of 150–200 °C (Bish, 1987) and a similar T is indicated by the presence of interstratified illite–smectite in the Central level (Pusch and Karnland, 1996; Vidal et al., 2012). Similarly, the association muscovite/illite, interstratified illite–smectite, and kaolinite of the Lateral level can be interpreted as a product of hydrolytic alteration at T from about 250 to 150 °C (Hedenquist and Arribas, 2022). These interpreted temperatures, in combination with the textural evidence for clay minerals replacing the retrograde skarn association (Fig. 4ce), are an indication that at Terranera the clay minerals formed at the late stages of ore formation. The environment of formation of this association is consistent with that of an epithermal intermediate- to low-sulfidation argillic system (Berger and Henley, 1989; Hedenquist and Arribas, 2000), while the smectite 2W-vermiculite-sepiolite association is indicative of a low-T weathering environment.

Notably, although late-stage argillic alteration is not typical of Fe-skarn deposits, an ore environment similar to that described here was documented in the Fe skarn deposit of Bizmişen, Turkey, which is a magnetite, hematite, goethite, pyrite, chalcopyrite skarn showing a quartz-illite-interstratified chlorite/smectite-interstratified illite/smectite-smectite association (Bozkaya et al., 2019). This was interpreted as a product of intermediate-sulfidation argillic alteration developed at the last stages of the Fe-skarn formation.

Interestingly, at Terranera there is a significant overlap between the temperature range of quartz-chlorite formation (180–350 °C), that of Thtot of the studied FIAs (260–325 °C), and the temperature range of goethite-argillic alteration. This overlap provides a strong indication that Fe oxide precipitation at Terranera started at c. 350 °C and carried on at lower temperatures until goethite and clay mineral precipitation. Intersecting the calculated isochores of the fault fluid with the 350 °C

isotherm of Fe oxide precipitation - i.e., considering the 350 °C quartz-chlorite temperature an independent constraint on ore precipitation – we calculate a range of fluid pressures of 27–125 MPa within the fault (Fig. 11b), which corresponds to a maximum lithostatic load of 1–4.7 km (considering an average crustal density of 2.7 g cm^{-3}).

The stability of the Fe-oxide and Fe-sulfide association at 350 °C can be used to construct a geochemical model of ore precipitation. These conditions are exemplified in Fig. 12a, which shows possible paths of ore deposition within the fault at a pressure of 50 MPa and as a function of a_{O2} and a_{H2S} in the fluid. For comparison, the stability fields of this assemblage at 300 °C/50 MPa (marked by dotted lines of Fig. 12a) have been added to evaluate the effects of cooling on these equilibria. Accordingly, an ore fluid initially in equilibrium with magnetite and pyrrhotite at 350 °C must change its properties to allow magnetite-pyrite, and eventually hematite-pyrite, and hematite precipitation. These changes corresponded to oxidation coupled with desulfidation (red paths of Fig. 12a) and must have occurred since the start of fluid mixing. Hence, following an initial stage of magnetite-pyrrhotite deposition at depth, the properties of the ore fluid varied to allow magnetite-pyrite, magnetite (Fig. 4b), hematite-pyrite (Fig. 4f), and hematite formation. Ore precipitation could have occurred at 350 °C if the fluid a_{O2} increased by at least 2 orders of magnitude to reach hematite supersaturation. However, supersaturation could have occurred also with a lower level of oxidation from a fluid initially supersaturated in magnetite but cooling during its flow (lower path). Fig. 12a shows that a shift of these fluid-mineral equilibria at 300 °C would cause a considerable expansion of the hematite and pyrite stability fields, which would bring the fluid a_{O2} and a_{H2S} compatible only with pyrite, hematite-pyrite, or hematite equilibrium and efficiently suppress magnetite formation. These significant changes of fluid-mineral equilibria explain the juxtaposition of magnetite- vs hematite-dominated mineralization at the outcrop (and even sample) scale at Terranera.

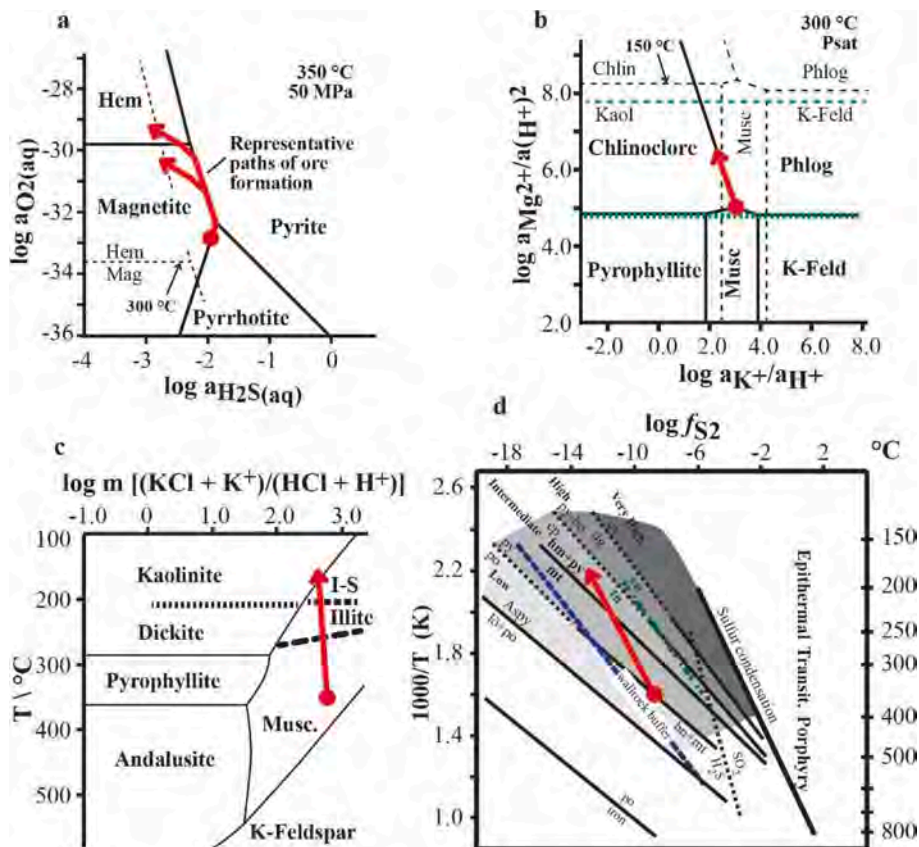The formation of the muscovite-phlogopite-clinochlore-talc

Fig. 12. Conditions of ore formation of the Terranera magnesian Fe-skarn. The trajectories in all panels are based on the gathered constraints and show possible evolutionary paths of the ore fluid. a. Stability diagram of Fe-oxides and pyrite calculated at 350 °C/50 MPa as a function of a_{O2} and a_{H2S}. The dotted lines show the shift of the stability fields at 300 °C and 50 MPa. b. Stability diagram of phyllosilicates in equilibrium with a H$_2$O-Cl fluid at 300 °C and saturated vapor pressure (from: Bowers et al., 1984). The dotted lines show the shift of the stability fields at 150 °C and P$_{sat}$. The green dotted lines mark the talc hydrolysis equilibrium Mg$_3$Si$_4$O$_{10}$(OH)$_2$ + 6H$^+$ = 3 Mg^{2+} + 4SiO$_{2(aq)}$ + 4H$_2$O. c. Experimentally based, temperature-log m(K/H) diagram showing the stability fields of K silicates and clay minerals resulting from hydrolytic alteration (from: Hedenquist and Arribas, 2022). d. Temperature-log f$_{S2}$ diagram showing sulfidation states of distinct ore assemblages from the porphyry-epithermal environments (modified after: Hedenquist and Arribas, 2022). Abbreviations: Asp = arsenopyrite; bn = bornite; cp = chalcopyrite; dg = digenite; en = enargite; hm = hematite; lö=löllingite mt = magnetite; po = pyrrhotite; py = pyrite; tn = tennantite. (For interpretation of the references to color in this figure legend, the reader is referred to the web version of this article.)

association is consistent with the skarn formation at the estimated temperatures. Equilibrium between these minerals and the ore fluid at 300 °C (Fig. 12b) shows that their occurrence in the Central level must have occurred at the invariant muscovite-clinochlore-phlogopite conditions, which identify unique a_{K+}/a_{H+} and $a_{Mg2+}/(a_{H+})^2$ values. A specific constraint was given by the presence of talc in the mineral assemblage, which was possible only at $a_{Mg2+}/(a_{H+})^2$ defined by talc hydrolysis, i.e., above the green dotted line of Fig. 12b. Clinochlore-phlogopite precipitation in absence of muscovite must have followed the univariant equilibrium conditions (arrow). Similarly to what is shown for the ore minerals, cooling of the ore fluid caused a significant expansion of the clay mineral stability field. Thus, a fluid initially in equilibrium with clinochlore and phlogopite at 300 °C would precipitate only kaolinite after cooling at 150 °C. A similar process must have occurred to allow kaolinite alteration in the Lateral level (Fig. 4e).

Experimentally determined conditions of illite, illite–smectite, and kaolinite formation from the alteration of K silicates (Fig. 12c) provide independent constraints on the transition from ore precipitation to late argillic alteration. Considering temperature and a_{K+}/a_{H+} as the main parameters that controlled this alteration at Terranera, and considering that in the Base, Central, and Lateral levels no dickite was detected in the studied samples but only illite, illite/smectite, and kaolinite, a specific pathway of hydrolytic alteration is defined. This pathway starts approximately at 350 °C, i.e., the T at which Fe-oxide precipitation started, and is directed along a cooling path without significant modification of the fluid a_{K+}/a_{H+} due to mineral buffering (e.g., red path along clinochlore-phlogopite buffer, Fig. 12c).

6.3. Model of ore deposition

Our model is consistent with the genesis of Terranera as a magnesian Fe skarn, which formed after interaction between distinct batches of hydrothermal fluids and the fault protoliths. These fluids mixed and cooled during their reactive flow while they formed the ore bodies within the fault zone and the hanging wall block. Argillic alteration of the fault rocks was a peculiar trait of this ore body and was probably controlled by the pristine abundance of phyllosilicates and feldspars in the protoliths, similar to what is described in the Fe skarn deposit of Bizmişen, Turkey (Bozkaya et al., 2019). The focused flow of the ore fluids within the fault – which is highlighted by the poor alteration of the footwall – contributed probably to the efficient argillification of fault rocks and hanging wall. The evolutionary path of this fluid during the ore- and late-stage precipitation was buffered by the wallrocks and fit the intermediate sulfidation conditions (Fig. 12d).

Finally, the EPMA (Table A8) and LA-ICP-TOFMS element imaging (Figs. 8 and A3) on the composition of hematite from the Base and Upper levels provide a set of constraints that are new for the Fe deposits of Elba and other skarns. Analysis based on the discriminant parameters of Dupuis and Beaudoin (2011) shows that the ranges of Ti + V and Ca + Al + Mn mass fractions (Table 3) overlap those defined for hematite from IOCG and porphyry deposits. This suggests that the Terranera hematite is distinct from that of a typical Fe-skarn. Such claim is confirmed by the concentration ranges of the trace elements Sb, Ga, Ge, and As (50–200 µg/g), which integrate the dataset based on EPMA. This group of elements is well known for being transported as aqueous species in

Table 3
Discriminant parameters for the Terranera hematite.

Discriminant Parameters	Range
Ti + V (wt.%)	0.04–0.19
Ca + Al + Mn (wt.%)	0.14–0.22
Al/(Zn + Ca)	3.2–4.3
Si + Mg (wt.%)	0.08–0.27

Note: data based on Table A8 of Appendix and on LA-ICP-TOFMS (Figs. 8, A3).

geothermal fluids (Barnes and Seward, 1997) or hosted within sulfides and ore minerals of epithermal deposits (Cook et al., 2009). Their concentration within these minerals is similar to that documented here for the Terranera hematite. This suggests that the range of ore composition at Terranera could be transitional between that of a typical skarn and that of a geothermal/epithermal deposit.

6.4. Metallogenic framework of Terranera

Other Fe deposits of the island of Elba show structural and geochemical characteristics that are akin to those shown here for Terranera. These characteristics include a dolomite-rich fault rock lithology and similar magnesian Fe skarn and epithermal mineral associations, which together suggest a similar genetic process. Notably, these characteristics were documented in fault-hosted, massive pyritic ore deposits of the Tuscan district, which have a Neogene age like those of the Elba deposits. This suggests that a transitional skarn/epithermal ore environment could have developed in other areas of southern Tuscany in the same geological period.

Faults and folds have long been considered essential for the genesis of the mineral deposits of Elba. The first pioneering studies determined very clearly a set of local faults and folds as the loci for the formation of the large hematite-pyrite ore bodies of Rio Marina (Fig. 1), especially those of the Bacino-Valle Giove stopes (Debenedetti, 1952; Gilliéron, 1959; Lotti, 1910; Stella, 1921). Similar considerations were made for the fault-hosted, hematite-pyrite-limonite ore bodies outcropping close to Terranera (Ortano, Capo d'Arco, Punta delle Cannelle: Cocco and Garavelli, 1953; Gottardi, 1962; Trevisan, 1950). Here, the ore minerals replaced the dolomitic marbles embedded within the local faults. A detailed structural, petrographic, mineralogical, and fluid inclusion study on the hematite-pyrite deposit of Rio Marina carried out by Deschamps et al (1983a, 1983b) showed that the Valle Giove ore bodies were hosted by a cataclastic dolostone embedded within N 110–130 E-striking faults (Table 4). The mineral association of these faults was the low-sulfidation epithermal adularia-epidote-talc-quartz-calcite association and was interpreted as the product of de-dolomitization of the protolith from hydrothermal fluids having variable salinities and a temperature between 320 and 280 °C.

With a cumulative historical production of c. 66 Mt of pyrite between 1861 and 1994 (ISTAT, 1995), the fault-hosted, massive pyritic ore deposits of south Tuscany represented an important ore district of Italy and Europe (Jenks, 1975). Pyrite was produced by eight deposits, namely Gavorrano, Niccioleta, Campiano, Boccheggiano, Fenice Capanne, Ritorto, M.te Argentario, and Isola del Giglio (Arisi Rota and Vighi, 1971). The first and largest of these deposits formed close to the 4.4 ± 0.6 Ma Gavorrano intrusion (Serri et al., 2001); i.e. a shallow level monzo- to leucogranite that emplaced synkinematically at the core of a thrust anticline whose geometry was strongly controlled by a back thrust and a forethrust fault (Mazzarini et al., 2004; Musumeci et al., 2005). The Gavorrano deposit was made of five ore bodies (Table 4) whose locations and compositions were controlled by two major faults (Gavorrano and Monticello faults: Arisi Rota and Vighi, 1971). Underground mine documentation shows that the Monticello fault hosted an epithermal ore body made of marcasite, realgar, antimonite, fluorite, barite, and quartz (Arisi Rota and Vighi, 1971). Of relevance is the fact that the Gavorrano fault bordering the western limb of the intrusion hosted a pyrite-pyrrhotite ore body associated with a prograde wollastonite-tremolite-andradite skarn and a retrograde quartz-chlorite-clay minerals-calcite skarn. Also, one of the protoliths of the Gavorrano ore body was a dolomitic marble, clay minerals were reported as abundant close to the ore body, and pyrite was determined as early in the paragenetic history (Arisi Rota and Vighi, 1971; Filippi and Masotti, 1980; Leonardelli, 1975; Radice, 1961). In this deposit, the ranges of δ^{34}S of pyrite (average: +9.3 ‰; range: +3.5 ÷ 12.4 ‰), sphalerite, galena, and chalcopyrite (range δ^{34}S: +6.2 ÷ +9.3 ‰) were used as isotopic geothermometers to determine skarn formation temperatures

Table 4
Characteristics of some fault-hosted ore deposits from the Island of Elba and the Tuscan district.

Deposit	Causative intrusion	Protoliths	Faults	Fault rocks	Main ore minerals	Gangue minerals	References
Terranera	Porto Azzurro monzogranite	Calamita Schists; Spotted Schists; Dolomitic marbles	Zuccale	Poorly foliated cataclasites; Dolomitic marble;	Hematite; Magnetite; Pyrite	Diopside; Spinel; Amphibole; Phlogopite; Chlorite; Talc, Tremolite; Quartz; Clay minerals	This work
Rio Marina (Valle Giove)	Porto Azzurro monzogranite	Dolostone (Carbonates Bréchoïdes)	Strike: N 110–130 E Dip: 70–90 NE	Cataclasite	Hematite; Pyrite	Adularia; Epidote; Chlorite; Talc; Quartz	1, 2
Gavorrano Group: Gavorrano, Rigoloccio, Ravi Marchi, Ravi Montecatini, Valmaggiore.	Gavorrano quartz-monzonite	Norian-Raethian dolomitic marble; Calcitic marble; Qtz monzonite; Microgranite dikes	Gavorrano; Monticello	Cataclastic dolostone/limestone; Fault breccias and gouges with limestone clasts.	Gavorrano fault: Pyrite; Pyrrhotite Monticello fault: Marcasite; Realgar; Antimonite.	Gavorrano: Wollastonite; Diopside; Tremolite; Andradite; Quartz; Chlorite; Clay minerals; Calcite Monticello fault: Fluorite; Barite; Quartz	3, 4, 5, 6
Fenice Capanne	Gavorrano quartz-monzonite	Norian-Raethian dolomitic limestone; Phyllites; Cretaceous-Eocene claystones	Accesa (Serrabottini); Fenice	Sulfide-and silicate-bearing veins	Pyrite; Sphalerite; Chalcopyrite; Galena ± Arsenopyrite; Cu-Sb-As sulfosalts; Hematite; Magnetite; Bismuthinite	Hedenbergite; Epidote; Quartz; Chalcedony; Calcite; Illite/Muscovite; Corrensite ± Ilvaite;	3, 7, 8, 9

Notes: The mineral composition reported for each fault rock represents a *mineral association* (sensu: Einaudi et al., 2003; Hedenquist and Arribas, 2022). See text for more details.
1: Gilliéron (1959); 2: Deschamps et al. (1983a; 1983b); 3: Arisi Rota and Vighi (1971); 4: Leonardelli (1975); 5: Filippi and Masotti (1980); 6: Radice (1961); 7: Dill (1979a, 1979b, 1980); 8: Fabris and Omenetto (1971); 9: Corsini et al. (1975).

between 430 ± 30 °C and 280 ± 30 °C (Tanelli and Lattanzi, 1983). All the features listed above are similar to those observed at Terranera and constitute a common trait of these deposits.

The Fenice Capanne massive deposit of south Tuscany showed very clearly a low-sulfidation epithermal assemblage associated with a typical skarn assemblage (Arisi Rota and Vighi, 1971; Corsini et al., 1975; Dill, 1979b; Dill, 1980; Fabris and Omenetto, 1971). This deposit consisted of two NNE- to NS trending and E-dipping faults (Accesa and Fenice) hosting a pyrite-rich ore and a zoned Zn-Pb-Cu mineralization (Fabris and Omenetto, 1971). The faults were up to 20 m in thickness (i. e., Poggio Bindo locality) but were segmented, with a pinch-and-swell structure, and showed a well-banded texture. They crosscut claystones and marls (Argille Scagliose), dolomitic limestone and evaporites (Norian-Raethian Calcare Cavernoso), and quartz-dolomite-albite phyllites and metagreywackes (Paleozoic Filladi di Boccheggiano). In some locations, the host rocks showed intense silicification (e.g., Argille Scagliose at Val Calda). The fault-hosted mineralization varied sub-stantially at different stopes and consisted of pyrite associated with variable proportions of pyrrhotite, sphalerite, chalcopyrite, galena, tetrahedrite, boulangerite and minor arsenopyrite, bismuthinite, and native Bi. The gangue consisted of a hedenbergite-epidote (±ilvaite) prograde skarn replaced by a retrograde quartz-calcite-chalcedony-sericite-clay mineral association. Dill (1979b, 1980) documented the presence of adularia-calcite-muscovite/illite-corrensite in the retro-grade skarn, and Corsini et al (1975) used electron probe microanalyses of sphalerites to calculate a range of mol% of FeS varying between 2.2 and 21.2. We stress that the pyrite-pyrrhotite-arsenopyrite-Cu-Sb-As sulfosalts ore association, the Fe-rich sphalerite, the banded vein tex-tures, the wallrock silicification, and the chalcedony-adularia-muscovite-clay minerals-calcite alteration of Fenice Capanne are all in agreement with formation in a low-sulfidation epithermal environment (Hedenquist and Arribas, 2000).

Hence, the proposed transitional skarn/epithermal nature of Terra-nera and of other fault-hosted, massive pyritic ore deposits of south Tuscany fits many observations gathered at distinct scales. This model reconciles some fundamental conflicts between the available data and the typical expected features of Fe skarns (Meinert et al., 2005). Indeed, key features of magnesian skarn deposits include their typical associa-tion with hypabyssal stocks and dikes of intermediate compositions (diorite, granodiorite, tonalite, syenite, and monzonite) within volcanic arcs (Baghban et al., 2021; Einaudi et al., 1981; Rubin and Kyle, 1998), the formation of magnetite (as opposed to hematite) as main ore min-eral, and the evidence for pyrite and pyrrhotite postdating magnetite. None of these typical features are found at Elba and in south Tuscany, showing that this model alone does not fit all the observations. On the other hand, a transitional skarn/epithermal environment occurring at the regional scale agrees with the documented presence of small epi-thermal precious-metal deposits in south Tuscany (Lattanzi, 1999; Sil-litoe and Brogi, 2021) and with the strikingly homogeneous δ^{34}S of the massive pyritic ore deposits of south Tuscany (mostly between +8.7 and +9.9 ‰: Tanelli and Lattanzi, 1983). It is also not in contrast with the extraction of Fe from the sulfide-bearing mica schists forming the Paleozoic basement rocks to form the deposits, as proposed by previous studies (Deschamps et al., 1983a; Deschamps et al., 1983b; Mazzarini et al., 2019; Tanelli and Lattanzi, 1986).

Open questions regarding this model are the relations between the ages of faulting and of the skarn/epithermal ore at Terranera. The available constraints fix the timing of the ZF activity at <5 Ma (Viola et al., 2022; Viola et al., 2018), i.e., after the out-of-sequence thrusting occurring at 4.9 ± 0.27 Ma. This age is slightly younger than that of Rio Marina (5.4–5.6 Ma, Wu et al., 2019). Combining this constraint with the ages of the Porto Azzurro pluton and of its metamorphic aureole (i.e., 6.53–5.9 and 6.76–6.23 Ma, respectively: Gagnevin et al., 2011; Maineri et al., 2003; Musumeci et al., 2015; Musumeci et al., 2011; Spiess et al., 2021), we conclude that the hydrothermal fluid of Terranera could not be generated by the adjacent Porto Azzurro – which was cold and crosscut by the ZF at that time. The causative pluton could have been a deeper magmatic body, maybe a deeper section of Porto Azzurro itself, which was at a late-crystallizing stage during the late Pliocene. The existence of such magmatic body can only be speculated at Terranera,

but it is reasonable to assume considering that the intrusive magmatism of the Island of Elba involved a mixing of shallow crustal magmas and mafic-intermediate melts generated deeper in the mantle (Poli and Peccerillo, 2016).

7. Conclusions

The range of hydrothermal processes documented at Terranera indicates that the ZF focused hydrothermal fluids, hosted ore-formation, and was the locus of permanent alteration/reworking of the fault rocks since the inception of ore formation. The sequence of processes that led to formation and alteration of the skarn minerals is useful in defining the ore deposit model.

Part of the dataset presented here is consistent with the genesis of Terranera as a magnesian Fe-skarn. The intense intermediate argillic alteration and the quantification within hematite of a group of elements that are characteristic of epithermal deposits represent features that are unusual in skarn deposits and suggest an ore environment that is transitional between that of a skarn and of a low- to intermediate-sulfidation epithermal deposit. We show that these compositional features are not characteristic of Terranera alone but are found in other representative deposits of Elba and south Tuscany showing similar characteristics and setting. This implies that this ore environment could have occurred beyond the Fe deposits of eastern Elba and characterized a much larger ore district in the Neogene.

Declaration of Competing Interest

The authors declare that they have no known competing financial interests or personal relationships that could have appeared to influence the work reported in this paper.

Data availability

Data will be made available on request.

Acknowledgements

Appendix A. Supplementary data

Supplementary data to this article can be found online at https://doi.org/10.1016/j.oregeorev.2023.105348.

References

Arisi Rota, F. and Vighi, L., 1971. Le mineralizzazioni a pirite ed a solfuri misti della Toscana meridionale, La Toscana Meridionale. Fondamenti geologico minerari per una prospettiva di valorizzazione delle risorse naturali. Società Italiana di Mineralogia e Petrologia, pp. 368-423.

Baghban, S., Zandi, Z., Lentz, D.R., 2021. Formation and evolution of the calcic-magnesian Saheb Fe(Cu) skarn deposit from the Sanandaj-Sirjan Belt, NW Iran: Evidence for multistage boiling in episodes of magnetite saturation. J. Geochem. Explor. 226, 106781.

Bakker, R.J., 2003. Package FLUIDS 1. Computer programs for analysis of fluid inclusion data and for modelling bulk fluid properties. Chem. Geol. 194 (1–3), 3–23.

Barnes, H.L., Seward, T.M., 1997. Geothermal systems and mercury deposits. In: Barnes, H.L. (Ed.), Geochemistry of Hydrothermal Ore Deposits. John Wiley and Sons, pp. 699–736.

Becker, F., Eser, R., Hoelzmann, P., Schütt, B., 2019. Reconstructing human–landscape interactions in the context of ancient iron smelting on Elba Island, Italy, using sedimentological evidence. Geoarchaeology 34 (3), 336–359.

Berger, B.R., Henley, R.W., 1989. Advances in the understanding of epithermal gold-silver deposits, with special references to the Western United States. Econ. Geol. Monograph 6, 405–423.

Bish, D.I., 1987. Smectite Dehydration and Stability: Applications to Radioactive Waste Isolation at Yucca Mountain. Los Alamos National Laboratory, Nevada.

Bourdelle, F., Cathelineau, M., 2015. Low-temperature chlorite geothermometry: a graphical representation based on a T-R^{2+}–Si diagram. Eur. J. Mineral. 27 (5), 617–626.

Bowers, T.S., Jackson, K.J., Helgeson, H.C., 1984. Equilibrium Activity Diagrams For Coexisting Minerals and Aqueous Solutions at Pressures and Temperatures to 5 kb and 600 °C. Springer Verlag.

Bozkaya, Ö., Bozkaya, G., Yılmaz, H., Hozatlıoğlu, D., Banks, D.A., 2019. The origin, age and duration of hydrothermal alteration associated with iron skarn mineralization determined from clay/phyllosilicate minerals, Bizmişen-Erzincan, East-Central Turkey. Ore Geol. Rev. 115, 103179.

Cocco, G., Garavelli, C., 1953. Studio di alcuni problemi geochimici relativi al giacimento di ferro di Capo Calamita (Elba). Rendiconti della Società Italiana di Mineralogia e Petrografia 10, 269–350.

Collettini, C., Holdsworth, R.E., 2004. Fault zone weakening and character of slip along low-angle normal faults: insights from the Zuccale fault, Elba, Italy. J. Geol. Soc. London 161, 1039–1051.

Cook, N.J., Ciobanu, C.L., Pring, A., Skinner, W., Shimizu, M., Danyushevsky, L., Saini-Eidukat, B., Melcher, F., 2009. Trace and minor elements in sphalerite: A LA-ICPMS study. Geochim. Cosmochim. Acta 73 (16), 4761–4791.

Corsini, F., Lattanzi, P., Tanelli, G., 1975. Contenuto in Fe delle blende del giacimento a solfuri di Cu, Pb e Zn di Fenice Capanne (Massa Marittima - Toscana), condizioni ambientali di formazione. Rendiconti della Società Italiana di Mineralogia e Petrografia, XXXI, pp. 351–364.

Debenedetti, A., 1952. Osservazioni sui giacimenti di pirite all'Elba. Bollettino del Servizio Geologico d'Italia 74, 53–85.

Deschamps, Y., Dagallier, G., Macaudiere, J., Marignac, C., Saupe, F., 1983a. Le gisement de pyrite-hématite de Valle Giove (Rio Marina, Ile d'Elbe, Italie): (Contribution à la connaissance des gisements de Toscane - I), Partie 1. Schweiz. Mineral. Petrogr. Mitt. 63, 149–165.

Deschamps, Y., Mecaudiere, J., Marignac, C., Moine, B., Saupe, F., 1983b. Le gisement de pyrite-hématite de Valle Giove (Rio Marina, Ile d'Elbe, Italie): (Contribution à la connaissance des gisements de Toscane -I), Partie 2. Schweiz. Mineral. Petrogr. Mitt. 63, 301–327.

Diakonov, I., Khodakovsky, I., Schott, J., Sergeeva, E., 1994. Thermodynamic properties of iron oxides and hydroxides; I, Surface and bulk thermodynamic properties of goethite (alpha -FeOOH) up to 500 K. Eur. J. Mineral. 6 (6), 967–983.

Dill, H., 1979a. Die Strahlenblende von Accesa. Tschermaks Mineral. Petrogr. Mitt. 26, 271–278.

Dill, H., 1979b. Lagerstättenkundliche Untersuchungen zur Entstehung der Pyrit-führenden Blei-Kupfer-Zink-Lagerstätte Accesa (SW-Toskana). Miner. Deposita 14 (1), 57–80.

Dill, H., 1980. Die Silikatmineralisation auf der Pyrit fuehenden Blei-Kupfer-Zinc-Lagerstaette Accesa (SW Toskana). Erzmetall 33 (6), 335–339.

Dini, A., Innocenti, F., Rocchi, S., Tonarini, S., Westerman, D.S., 2002. The magmatic evolution of the late Miocene laccolith-pluton-dyke granitic complex of Elba Island, Italy. Geol. Mag. 139 (03), 257–279.

Dünkel, I., Kuhlemann, J., Nohlen, U., 2003. Iron ore formation and neotectonic evolution in Elba (Tuscany, Italy) during Messinian plutonism. Neues Jahrbuch für Geologie und Paläontologie - Abhandlungen 230 (2–3), 391–407.

Dupuis, C., Beaudoin, G., 2011. Discriminant diagrams for iron oxide trace element fingerprinting of mineral deposit types. Miner. Deposita 46 (4), 319–335.

Einaudi, M.T., Hedenquist, J.W. and Inan, E.E., 2003. Sulfidation state of fluids in active and extinct hydrothermal systems: transitions from porphyry to epithermal environments. In: S.F. Simmons (Editor), Volcanic, Geothermal, and Ore-Forming Fluids: Rulers and Witnesses of Processes within the Earth Special Publication. Society of Economic Geologists and Geochemical Society, pp. 285–313.

Einaudi, M.T., Meinert, L.D., Newberry, R.J., 1981. Skarn deposits. Econ. Geol. 75th Anniversary Volume, 317–391.

Fabris, B.B., Omenetto, P., 1971. Osservazioni sul giacimento filoniano a solfuri di Zn, Pb e Cu di Fenice Capanne presso Massa Marittima (Toscana). Rendiconti della Società Italiana di Mineralogia e Petrografia, XXVII, pp. 393–435.

Filippi, L., Masotti, A., 1980. Breve nota illustrativa della campagna di sondaggi 1980 nella Massa Boccheggiano e calcolo delle riserve al di sotto del livello -224. SolMine SpA, Follonica.

Gagnevin, D., Daly, J.S., Horstwood, M.S.A., Whitehouse, M.J., 2011. In-situ zircon U-Pb, oxygen and hafnium isotopic evidence for magma mixing and mantle metasomatism in the Tuscan Magmatic Province, Italy. Earth Planet. Sci. Lett. 305 (1), 45–56.

Garofalo, P.S., Matthäi, S.K., Heinrich, C.A., 2002. Three-dimensional geometry, ore distribution, and time-integrated mass transfer through the quartz-tourmaline-gold vein network of the Sigma deposit (Abitibi belt - Canada). Geofluids 2, 217–232.

Gilliéron, F., 1959. Osservazioni sulla geologia dei giacimenti di ferro dell'Elba orientale. Industria Mineraria X(1), 1–10.

Goldstein, R.H., Reynolds, T.J., 1994. Fluid inclusion microthermometry. In: Goldstein, R.H. (Ed.), Systematics of Fluid inclusions in Diagenetic Minerals - SEPM Short Course 31. SEPM (Society for Sedimentary Geology), Tulsa, Oklahoma, pp. 87–121.

Gottardi, G., 1962. Solfuri ed ossidi di ferro del giacimento di Ortano (Isola d'Elba). Atti della Società Toscana di Scienze Naturali A69, 327–341.

Groves, D.I., Santosh, M., Goldfarb, R.J., Zhang, L., 2018. Structural geometry of orogenic gold deposits: Implications for exploration of world-class and giant deposits. Geosci. Front. 9 (4), 1163–1177.

Gundlach-Graham, A., Garofalo, P.S., Schwarz, G., Redi, D., Günther, D., 2018. High-resolution, quantitative element imaging of an upper crust, low-angle cataclasite (Zuccale Fault, Northern Apennines) by laser ablation ICP time-of-flight mass spectrometry. Geostand. Geoanal. Res. 42 (4), 559–574.

Hedenquist, J.W., Arribas R., A., Gonzalez-Urien, E., Hagemann, S.G., Brown, P.E., 2000. Exploration for Epithermal Gold Deposits, Gold in 2000. Society of Economic Geologists, pp. 245-277.

Hedenquist, J.W., Arribas, A., 2022. Exploration implications of multiple formation environments of advanced argillic minerals. Econ. Geol. 117 (3), 609–643.

Istat, 1995. Produzione di miniere e cave. Istituto Centrale di Statistica, Rome, Italy.

Jenks, W.F., 1975. Origins of some massive pyritic ore deposits of western Europe. Econ. Geol. 70 (3), 488–498.

Keller, J.V.A., Coward, M.P., 1996. The structure and evolution of the Northern Tyrrhenian Sea. Geol. Mag. 133 (1), 1–16.

Keller, J.V.A., Pialli, G., 1990. Tectonics of the island of Elba: A reappraisal. Bollettino della Società Geologica Italiana 109, 413–425.

Lattanzi, P., 1999. Epithermal precious metal deposits of Italy - an overview. Miner. Deposita 34, 630–638.

Leake, B.E., Woolley, A.R., Arps, C.E.S., Birch, W.D., Gilbert, M.C., Grice, J.D., Hawthorne, F.C., Kato, A., Kisch, H.J., Krivovichev, V.G., Linthout, K., Laird, J., Mandarino, J., Maresch, W.V., Nickel, E.H., Rock, N.M.S., Schumacher, J.C., Smith, D.C., Stephenson, N.C.N., Ungaretti, L., Whittaker, E.J.W., Youzhi, G., 2018. Nomenclature of Amphiboles; Report of the Subcommittee on Amphiboles of the International Mineralogical Association Commission on New Minerals and Mineral Names. Mineral. Mag. 61 (405), 295–310.

Leonardelli, A., 1975. Ricerche effettuate nella miniera di Gavorrano tra il giugno 1974 ed il maggio 1975, Rimin SpA.

Lippolt, H.J., Wernicke, R.S., Baehr, R., 1995. Paragenetic specularite and adularia (Elba, Italy): Concordant (U + Th)-He and K-Ar ages. Earth Planet. Sci. Lett. 132 (1), 43–51.

Lotti, B., 1910. I giacimenti metalliferi in relazione colle rocce eruttive mioceniche. In: Lotti, B. (Ed.), Geologia Della Toscana. Regio Ufficio Geologico, Roma, pp. 303–310.

Maineri, C., Benvenuti, M., Costagliola, P., Dini, A., Lattanzi, P., Ruggieri, G., Villa, I.M., 2003. Sericitic alteration at the La Crocetta deposit (Elba Island, Italy): interplay between magmatism, tectonics and hydrothermal activity. Miner. Deposita 38 (1), 67–86.

Majzlan, J., Grevel, K.-D., Navrotsky, A., 2003a. Thermodynamics of Fe oxides: Part II. Enthalpies of formation and relative stability of goethite (α-FeOOH), lepidocrocite (γ-FeOOH), and maghemite (γ-Fe2O3). Am. Mineral. 88 (5–6), 855–859.

Majzlan, J., Lang, B.E., Stevens, R., Navrotsky, A., Woodfield, B.F., Boerio-Goates, J., 2003b. Thermodynamics of Fe oxides: Part I. Entropy at standard temperature and pressure and heat capacity of goethite (α-FeOOH), lepidocrocite (γ-FeOOH), and maghemite (γ-Fe2O3). Am. Mineral. 88 (5–6), 846–854.

Marinelli, G., 1959. Le intrusioni terziarie dell'Isola d'Elba. Atti della Società Toscana di Scienze Naturali, LXVI, pp. 50–250.

Massa, G., Musumeci, G., Mazzarini, F., Pieruccioni, D., 2016. Coexistence of contractional and extensional tectonics during the northern Apennines orogeny: the late Miocene out-of-sequence thrust in the Elba Island nappe stack. Geol. J. 52 (3), 353–368.

Mazzarini, F., Corti, G., Musumeci, G., Innocenti, F., Breitkreuz, C., Petford, N., 2004. Tectonic control on laccolith emplacement in the northern Apennines fold–thrust belt: the Gavorrano intrusion (southern Tuscany, Italy), Physical Geology of High-Level Magmatic Systems. Geological Society of London.

Mazzarini, F., Musumeci, G., Viola, G., Garofalo, P.S., Mattila, J., 2019. Structural and lithological control on fluid circulation, dilation and ore mineralization (Rio Albano mine, Island of Elba, Italy). J. Struct. Geol. 126, 210–230.

Meinert, L.D., Dipple, G.M., Nicolescu, S., 2005. World skarn deposits. Econ. Geol. volume 299–336.

Montecatini SpA, 1951. Ricerche all'Isola d'Elba. Relazione e carta geologica della zona di Terranera, Montecatini SpA internal report.

Muntean, J.L., Einaudi, M.T., 2001. Porphyry-epithermal transition: Maricunga belt, Northern Chile. Econ. Geol. 96, 743–772.

Musumeci, G., Mazzarini, F., Corti, G., Barsella, M., Montanari, D., 2005. Magma emplacement in a thrust ramp anticline: The Gavorrano Granite (northern Apennines, Italy). Tectonics 24 (6).

Musumeci, G., Mazzarini, F., Tiepolo, M., Di Vincenzo, G., 2011. U-Pb and ^{40}Ar-^{39}Ar geochronology of Palaeozoic units in the northern Apennines: determining protolith age and alpine evolution using the Calamita Schist and Ortano Porphyroid. Geol. J. 46 (4), 288–310.

Musumeci, G., Mazzarini, F., Cruden, A.R., 2015. The Zuccale Fault, Elba Island, Italy: A new perspective from fault architecture. Tectonics 34, 1195–1218.

Musumeci, G., Vaselli, L., 2012. Neogene deformation and granite emplacement in the metamorphic units of northern Apennines (Italy): Insights from mylonitic marbles in the Porto Azzurro pluton contact aureole (Elba Island). Geosphere 8, 470–490.

Oliver, N.H.S., Bons, P.D., 2001. Mechanisms of fluid flow and fluid-rock interaction in fossil metamorphic hydrothermal systems inferred from vein-wallrock patterns, geometry and microstructure. Geofluids 1, 137–162.

Papeschi, S., Musumeci, G., Mazzarini, F., 2017. Heterogeneous brittle-ductile deformation at shallow crustal levels under high thermal conditions: The case of a synkinematic contact aureole in the inner northern Apennines, southeastern Elba Island, Italy. Tectonophysics 817, 547–564.

Papeschi, S., Musumeci, G., Massonne, H.-J., Bartoli, O., Cesare, B., 2019. Partial melting and strain localization in metapelites at very low-pressure conditions: The northern Apennines magmatic arc on the Island of Elba, Italy. Lithos 350–351, 105230.

Papeschi, S., Ryan, E., Musumeci, G., Mazzarini, F., Garofalo, P.S., Viola, G., 2021. Geology of the Northern Apennines nappe stack on eastern Elba (Italy): new insights on the Neogene orogenic evolution of the Northern Tyrrhenian Sea. J. Maps 17 (2), 519–532.

Pertusati, P.C., Raggi, G., Ricci, C.A., Duranti, S., Palmeri, R., 1993. Evoluzione postcollisionale dell'Elba centro-orientale. Memorie della Società Geologica Italiana 49, 297–312.

Pieczka, A., Szuszkiewicz, A., Szeleg, E., Nejbert, K., Łodzinski, M., Ilnicki, S., Turniak, K., Banach, M., Holub, W., Michalowski, P., Rożniak, R., 2013. (Fe, Mn)-(Ti, Sn)-(Nb, Ta) oxide assemblage in a little fractionated portion of a mixed (NYF + LCT) pegmatite from Pilawa Gorna, the Sowie Mts. block, SW Poland. J. Geosci. 58 (2), 91–112.

Poli, G., Peccerillo, A., 2016. The Upper Miocene magmatism of the Island of Elba (Central Italy): compositional characteristics, petrogenesis and implications for the origin of the Tuscany Magmatic Province. Mineral. Petrol. 110 (4), 421–445.

Pusch, R., Karnland, O., 1996. Physico/chemical stability of smectite clays. Eng. Geol. 41 (1), 73–85.

Radice, L., 1961. Miniera di Gavorrano - rilievo geologico al -140, Montecatini SpA.

Report, 1944. Ferro - Miniere Terranera-Capobianco dal 1894 al 1943. Corpo Reale delle Miniere, Firenze.

Rossetti, F., Balsamo, F., Villa, I.M., Bouybaouenne, M., Faccenna, C., Funiciello, R., 2008. Pliocene-Pleistocene HT–LP metamorphism during multiple granitic intrusions in the southern branch of the Larderello geothermal field (southern Tuscany, Italy). J. Geol. Soc. London 165 (1), 247–262.

Rubin, J., Kyle, J., 1998. The Gunung Bijih Timur (Ertsberg East) skarn complex, Irian Jaya, Indonesia: geology and genesis of a large, magnesian, Cu-Au skarn. In: Lentz, D.R. (Ed.), Mineralized Intrusion-related Skarn Systems. Short Course Series. Mineralogical Association of Canada, Québec, Canada, pp. 245–288.

Ryan, E., Papeschi, S., Viola, G., Musumeci, G., Mazzarini, F., Torgersen, E., Sørensen, B. E. and Ganerød, M., 2021. Syn-Orogenic Exhumation of High-P Units by Upward Extrusion in an Accretionary Wedge: Insights From the Eastern Elba Nappe Stack (Northern Apennines, Italy). Tectonics, 40(5): e2020TC006348.

Serri, G., Innocenti, F., Manetti, P., 2001. Magmatism from Mesozoic to Present: petrogenesis, time-space distribution and geodynamic implications. In: Vai, G.B., Martini, I.P. (Eds.), Anatomy of an Orogen: the Apennines and Adjacent Mediterranean Basins. Springer, Netherlands, Dordrecht, pp. 77–103.

Seward, T.M., Barnes, H.L., 1997. Metal transport by hydrothermal ore fluids. In: Barnes, H.L. (Ed.), Geochemistry of Hydrothermal Ore Deposits. John Wiley & Sons, pp. 435–486.

Sillitoe, R.H., Brogi, A., 2021. Geothermal systems in the Northern Apennines, Italy: modern analogues of Carlin-style gold deposits. Econ. Geol. 116 (7), 1491–1501.

Smith, S.A.F., Holdsworth, R.E., Collettini, C. and Pearce, M.A., 2011. The microstructural character and mechanical significance of fault rocks associated with a continental low-angle normal fault: the Zuccale Fault, Elba Island, Italy. In: Å. Fagereng, V.G. Toy and J.V. Rowland (Editors), Geology of the Earthquake Source: A Volume in Honour of Rick Sibson. Geological Society, London, Special Publications, London, pp. 97-113.

Spiess, R., Langone, A., Caggianelli, A., Stuart, F.M., Zucchi, M., Bianco, C., Brogi, A., Liotta, D., 2021. Unveiling ductile deformation during fast exhumation of a granitic pluton in a transfer zone. J. Struct. Geol. 147, 104326.

Steele-MacInnis, M., Bodnar, R.J., Naden, J., 2011. Numerical model to determine the composition of H$_2$O–NaCl–CaCl$_2$ fluid inclusions based on microthermometric and microanalytical data. Geochim. Cosmochim. Acta 75 (1), 21–40.

Steele-MacInnis, M., Ridley, J., Lecumberri-Sanchez, P., Schlegel, T.U., Heinrich, C.A., 2016. Application of low-temperature microthermometric data for interpreting multicomponent fluid inclusion compositions. Earth Sci. Rev. 159, 14–35.

Stefansson, A., Lemke, K., Seward, T.M., 2008. Iron (III) complexation in hydrothermal solutions: An experimental and theoretical study, Water, steam and aqueous solutions: Advances in science and technology for power generation: Proceedings of the 15th International Conference on the Properties of Water and Steam, September 7-11, 2008, Berlin. Verein Deutscher Ingenieure VDI.

Stella, A., 1921. Le miniere di ferro dell'Italia. In: Stella, A. (Ed.), Primo Congresso Minerario Nazionale. Lattes & Co, Roma, pp. 183–259.

Tanelli, G., Lattanzi, P., 1983. Pyritic ores of southern Tuscany, Italy. In: J.P.R. DeVilliers (Editor), ICAM 81. Proceedings of the First International Congress on Applied Mineralogy. Geological Society of South Africa, Johannesburg, South Africa, pp. 315-323.

Tanelli, G., Benvenuti, M., Costagliola, P., Dini, A., Lattanzi, P., Maineri, C., Mascaro, I., Ruggieri, G., 2001. The iron mineral deposits of Elba island: state of the art. Ofioliti 26, 239–248.

Tanelli, G., Lattanzi, P., 1986. Metallogeny and mineral exploration in Tuscany: state of the art. Memorie della Società Geologica Italiana 31, 299–304.

Testemale, D., Brugger, J., Liu, W., Etschmann, B., Hazemann, J.-L., 2009. In-situ X-ray absorption study of Iron(II) speciation in brines up to supercritical conditions. Chem. Geol. 264 (1), 295–310.

Thompson, J.F.H., Sillitoe, R.H., Baker, T., Lang, J.R., Mortensen, J.K., 1999. Intrusion-related gold deposits associated with tungsten-tin provinces. Miner. Deposita 34, 323–334.

Trevisan, L., 1950. L'Elba orientale e la sua tettonica di scivolamento per gravità. Memorie Istituto di Geologia Università di Padova 16, 5–39.

Vidal, O., Baldeyrou, A., Beaufort, D., Fritz, B., Geoffroy, N., Lanson, B., 2012. Experimental Study of the Stability and Phase Relations of Clays at High Temperature in a Thermal Gradient. Clay Clay Miner. 60 (2), 200–225.

Viola, G., Torgersen, E., Mazzarini, F., Musumeci, G., Lelij, R., Schönenberger, J., Garofalo, P.S., 2018. New Constraints on the Evolution of the Inner Northern Apennines by K-Ar Dating of Late Miocene-Early Pliocene Compression on the Island of Elba, Italy. Tectonics 37 (3229–3243).

Viola, G., Musumeci, G., Mazzarini, F., Tavazzani, L., Curzi, M., Torgersen, E., van der Lelij, R., Aldega, L., 2022. Structural characterization and K-Ar illite dating of

reactivated, complex and heterogeneous fault zones: lessons from the Zuccale Fault, Northern Apennines. Solid Earth 13 (8), 1327–1351.

Whitney, D.L., Evans, B.W., 2010. Abbreviations for names of rock-forming minerals. American Mineralogist 95 (1), 185–187.

Wu, L.-Y., Stuart, F.M., Di Nicola, L., Heizler, M., Benvenuti, M., Hu, R.-Z., 2019. Multi-aliquot method for determining (U + Th)/He ages of hydrothermal hematite: Returning to Elba. Chem. Geol. 504, 151–157.